

Contextual inference underlies the learning of sensorimotor repertoires

<https://doi.org/10.1038/s41586-021-04129-3>

James B. Heald^{1,2,3}✉, Máté Lengyel^{2,4,5} & Daniel M. Wolpert^{1,2,3,5}

Received: 8 December 2020

Accepted: 13 October 2021

Published online: 24 November 2021

 Check for updates

Humans spend a lifetime learning, storing and refining a repertoire of motor memories. For example, through experience, we become proficient at manipulating a large range of objects with distinct dynamical properties. However, it is unknown what principle underlies how our continuous stream of sensorimotor experience is segmented into separate memories and how we adapt and use this growing repertoire. Here we develop a theory of motor learning based on the key principle that memory creation, updating and expression are all controlled by a single computation—contextual inference. Our theory reveals that adaptation can arise both by creating and updating memories (proper learning) and by changing how existing memories are differentially expressed (apparent learning). This insight enables us to account for key features of motor learning that had no unified explanation: spontaneous recovery¹, savings², anterograde interference³, how environmental consistency affects learning rate^{4,5} and the distinction between explicit and implicit learning⁶. Critically, our theory also predicts new phenomena—evoked recovery and context-dependent single-trial learning—which we confirm experimentally. These results suggest that contextual inference, rather than classical single-context mechanisms^{1,4,7–9}, is the key principle underlying how a diverse set of experiences is reflected in our motor behaviour.

Throughout our lives, we experience different contexts in which the environment exhibits distinct dynamical properties, such as when manipulating different objects or walking on different surfaces. Although the brain can maintain multiple motor memories that are appropriate for these contexts^{10,11}, classical theories of motor learning focus on how the brain adapts to a single environment^{1,7,8}. However, with multiple memories come new challenges—the brain must decide when to create new memories¹² and how much to express and update them for each movement. These operations, their governing principles and their consequences for motor learning remain poorly understood. We propose a unifying principle—contextual inference—that specifies how sensorimotor experience determines memory creation, expression and updating. We show that contextual inference is the core feature that underlies a range of fundamental aspects of motor learning that were previously explained by distinct and often heuristic processes.

The COIN model of motor learning

To formalize the role of contextual inference in motor learning, we developed the contextual inference (COIN) model, a Bayesian nonparametric model of motor learning (Methods). The COIN model is based on an internal model that specifies the learner's assumptions about how the environment generates sensory observations (Fig. 1a and Extended Data Fig. 1a). Motor learning corresponds to online inference under this generative model (Fig. 1b and Extended Data Fig. 1b). Specifically, the COIN model jointly infers contexts, their transitions, their dynamical and

sensory properties, and the current state of each context, with each motor memory storing the inferences about a different context (for validation; Extended Data Fig. 2a, b). The challenge is that neither contexts nor their transitions come labelled. Thus, the learner needs to continually infer the current context on the basis of a continuous stream of experience.

Contextual inference computes a posterior distribution expressing the probability that each known context, or a yet-unknown novel context, is currently active (Fig. 1b, top row) and thereby determines memory creation, expression and updating (Fig. 1b). Figure 1c–h and Extended Data Fig. 1c–e illustrate a simulation of the COIN model (the parameters are provided in Extended Data Fig. 3) when handling objects of varying weights. To determine the motor command (Fig. 1e, cyan line), rather than selecting a single memory to be expressed^{11,12}, the state associated with each memory (Fig. 1d) is expressed commensurate with the probability of the corresponding context under the posterior, computed after observing the sensory cue but before movement ('predicted probability'; Fig. 1b, f). After movement, the 'responsibility' of each known context as well as of a yet-unknown, novel context is computed as their posterior probability given both the cue and the resultant state feedback. A new memory is created whenever the responsibility of a novel context becomes high (Fig. 1b, g). Critically, context responsibilities also scale the updating of existing memories and any newly created memory (Fig. 1b, d, h; the red and pink arrows, respectively, show how high or low responsibility for the red context accelerates or decelerates the updating of its state). Finally, these responsibilities are used to compute the predicted context probabilities on the next time step (Fig. 1f).

¹Mortimer B. Zuckerman Mind Brain Behavior Institute, Columbia University, New York, NY, USA. ²Computational and Biological Learning Lab, Department of Engineering, University of Cambridge, Cambridge, UK. ³Department of Neuroscience, Columbia University, New York, NY, USA. ⁴Center for Cognitive Computation, Department of Cognitive Science, Central European University, Budapest, Hungary. ⁵These authors contributed equally: Máté Lengyel, Daniel M. Wolpert. ✉e-mail: jamesbheald@gmail.com

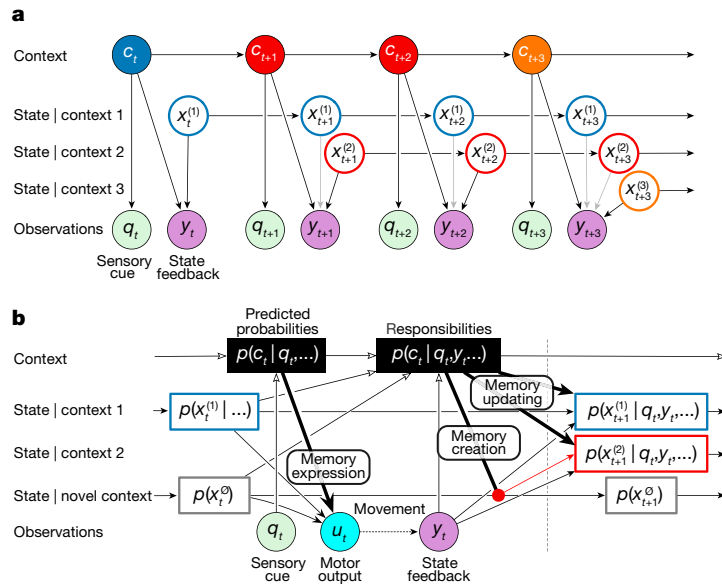
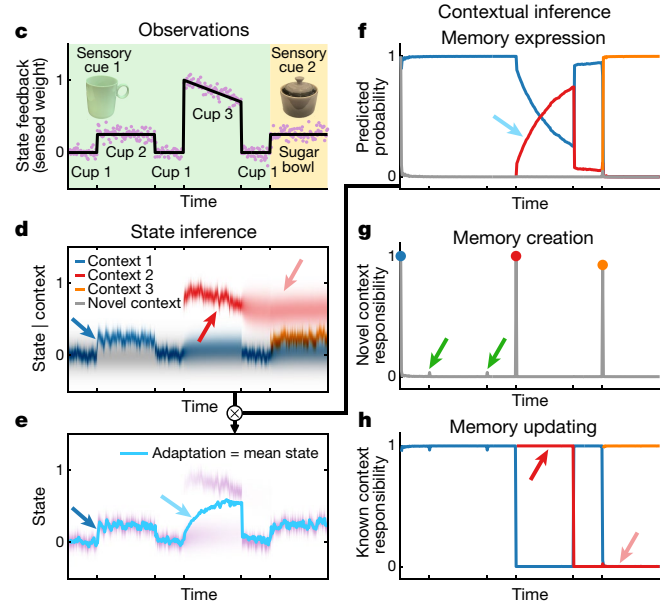


Fig. 1 | Contributions of contextual inference to motor learning in the COIN model. **a**, Generative model. A potentially infinite number of discrete contexts c_t (colours) exist with Markovian transitions. Each context j is associated with a time-varying state $x_t^{(j)}$. The active context can generate a sensory cue q_t , independent of movement (for example, object visual appearance) and also determines which state is observed (with noise) as state feedback y_t as a consequence of movement (for example, object weight, black versus grey arrows). **b**, Inference process. The learner infers contexts and states (and parameters, not shown) on the basis of the observed sensory cues and state feedback. Before movement, predicted context probabilities $p(c_t | q_t, \dots)$ are computed by fusing prior expectations from the previous time point (where ... refers to all observations before time t) with the likelihood of the current sensory cue q_t . For each known context, a predicted distribution over its current state $p(x_t^{(j)} | \dots)$ is represented. A potential novel context is always represented, with a stationary state distribution $p(x_t^{(0)})$. Motor output u_t is the average of the states of the known and novel contexts, weighted by their predicted probabilities ('memory expression'). Movement results in state feedback y_t , which updates the predicted context probabilities to context responsibilities $p(c_t | q_t, y_t, \dots)$. A new memory is instantiated with a probability that is the responsibility of the novel context ('memory creation' for a red context, initialized with the state distribution of the novel context). Responsibilities also determine the degree to



which state feedback is used to update the predicted state distribution $p(x_t^{(j)} | q_t, y_t, \dots)$ of each context ('memory updating'). **c**, Simulated time series of sensory cues (background colour for object appearance) and state feedback observations (noisy weight, purple) when handling visually identical cups and a sugar bowl of varying weights (black line, arbitrary scale). The weight of cup 3 decreases as liquid is poured from it, other objects have constant weights. **d-h**, The COIN model applied to the observations in **c**. **d**, Predicted state distributions for the three contexts inferred by the model and a novel context. **e**, The predicted state distribution (purple) is a mixture of the individual contexts' predicted state distributions (**d**) weighted by their predicted probabilities (**f**). The motor output (adaptation, cyan line) is the mean of the predicted state distribution. The intensity of the colours in **d** and the purple in **e** indicates probability density, linearly scaled between 0 and the maximum of the corresponding density. **f-h**, Contextual inferences (colours as described in **d**). **f**, The predicted probability (before state feedback) of each known context and a novel context. **g**, The responsibility (context probability after state feedback) of a novel context. The coloured circles show memory creation events. The novel context responsibility is insufficient to generate a new memory when transitioning to and from cup 2 (green arrows). **h**, The responsibility of each known context. The arrows in **d-f** and **h**, are explained in the main text (*The COIN model of motor learning*). For definitions of variables, see Methods.

In summary, the COIN model proposes that contextual inference is core to motor learning. In contrast to traditional models of learning, adaptation to a change in the environment (as in Fig. 1e, blue and cyan arrows) can arise from two distinct and interacting mechanisms. First, consistent with classical notions of learning, 'proper' learning constitutes the creation and updating of memories (the inferred states of known contexts; Fig. 1d, blue arrow). Second, 'apparent' learning occurs due to the updating of the predicted context probabilities (Fig. 1f, cyan arrow), thereby altering the extent to which existing memories are ultimately expressed in behaviour.

Apparent learning in memory recovery

To test the contributions of contextual inference to memory creation and expression (Fig. 1b), we revisited a widely used motor learning paradigm. In this paradigm (Fig. 2a and top left of Fig. 2b), participants learn a perturbation, P^+ , applied by a robotic interface while reaching to a target. Adaptation is assessed using occasional channel trials, P^- , which remove movement errors and measure the forces participants use to counteract the perturbation (Fig. 2a and Methods). Exposure to P^+ is followed by brief exposure to the opposite perturbation, P^- , bringing adaptation back, near to the baseline. Finally, a series of channel trials is administered. As

in previous studies¹, our participants showed the feature of spontaneous recovery in this phase (Fig. 2c): a transient re-expression of P^+ adaptation, rather than a simple decay towards the baseline.

Although this paradigm has no explicit sensory cues, according to our theory, contextual inference has an important role. When simulated for this paradigm (Fig. 2b), the COIN model starts with a memory that is appropriate for moving in the absence of a perturbation (P^0 ; Fig. 2b, bottom left) and creates new memories for the P^+ and P^- perturbations (red and orange, respectively). Spontaneous recovery arises due to the dynamics of contextual inference. As P^+ has been experienced on most trials, it is quickly inferred to be active with a high probability during the channel-trial phase (Fig. 2b, top right). As its state has not yet decayed (Fig. 2b, bottom left), the memory of P^+ is therefore transiently expressed in the motor output (Fig. 2b, bottom right). This mechanism is fundamentally different from a classical, single-context model of motor learning, the dual-rate model¹. In the dual-rate model, motor output is determined by a combination of individual memories that update at different rates (fast and slow) but of which the expression does not change over time. Thus, the dynamics of adaptation is solely determined by memory updating, that is, proper learning. By contrast, in the COIN model, changes in motor output can occur without updating any individual memory, simply due to changes in the extent to

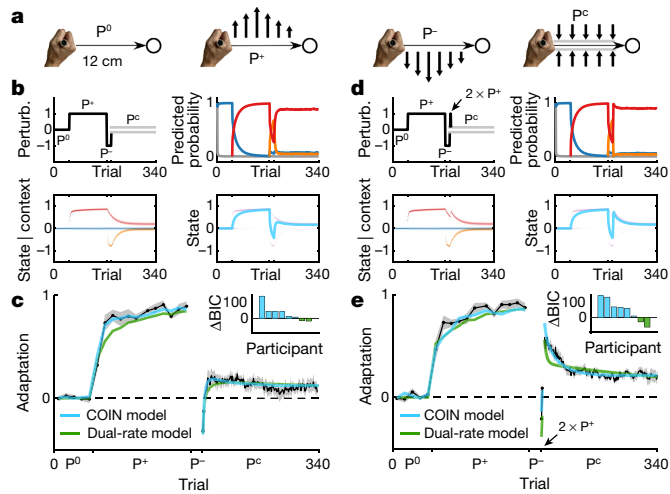


Fig. 2 | Memory creation and expression accounts for spontaneous and evoked recovery. **a**, Participants made reaching movements (thin horizontal arrows) to a target (circle) while holding the handle of a robotic manipulandum that could generate forces (thick vertical arrows). For clarity, the schematic is not to scale. The manipulandum could either be passive (null field, P^0) or generate a velocity-dependent force field that acted to the left (P^-) or right (P^+) of the current movement direction. Channel trials (P^c) were used to assess adaptation by constraining the hand to a straight channel (grey lines) to the target and measuring the forces generated by the participant into the virtual channel walls. **b**, Simulation of the spontaneous recovery paradigm with the COIN model (parameters fit to average data in **c** and **e** simultaneously). Top left, perturbation (Perturb., black) and channel-trial phase (grey). Bottom left, the predicted state distributions of inferred contexts as in Fig. 1d (for clarity we omit the novel context here and in subsequent figures). Note that full predicted state distributions are inferred but appear narrow owing to fitting to across-participant average data (see Methods). Top right, the predicted probability of contexts as in Fig. 1f. Bottom right, the predicted state distribution (purple) and its mean (cyan) as in Fig. 1e. **c**, Mean \pm s.e.m. adaptation (black, across $n = 8$ participants) on the channel trials of the spontaneous recovery paradigm. The cyan and green lines show model fits (mean of individual participant fits) of the COIN (7 parameters) and dual-rate models (5 parameters), respectively. Inset: Δ BIC (nats) for individual participants, positive favours the COIN model. **d**, **e**, Simulation of the evoked recovery paradigm with the COIN model (**d**) and the mean \pm s.e.m. adaptation on the channel trials of the evoked recovery paradigm (**e**) as described in **b** and **c**, respectively ($n = 8$ participants). The third and fourth trials in the channel-trial phase were replaced by P^+ trials (black arrow). The COIN model parameters are provided in Extended Data Fig. 3.

which existing memories are expressed due to contextual inference, that is, apparent learning. This mechanism enables the COIN model to account robustly for spontaneous recovery (Extended Data Fig. 4a), including elevated or reduced levels, respectively, when the P^+ phase is extended¹³ (Extended Data Fig. 5a–j) or when P^- is experienced before the P^+ phase¹⁴ (Extended Data Fig. 5k–o).

To distinguish between proper and apparent learning as the main mechanism underlying spontaneous recovery, we designed an ‘evoked recovery’ paradigm in which sensorimotor evidence clearly indicates that a change in context has occurred. For this, two early trials in the channel-trial phase of the spontaneous recovery paradigm were replaced with P^+ (evoker) trials (Fig. 2d, top left; similar to trigger trials in visuomotor learning¹¹ and reinstatement in conditioning¹⁵). In this case, the COIN model predicts a strong and long-lasting recovery of P^+ -adapted behaviour (Fig. 2d, bottom right and Extended Data Fig. 4b), primarily due to the inference that the P^+ context is now active (Fig. 2d, top right, red) and the gradual decay of the P^+ state over subsequent channel trials (Fig. 2d, bottom left, red). Our mathematical analysis suggested that these predictions for evoked recovery (as well

as those for spontaneous recovery) are inherent features of the COIN model (Supplementary Information and Extended Data Fig. 6a–c). By contrast, the dual-rate model predicts only a transient recovery that rapidly decays due to the same underlying adaptation process with fast dynamics governing both recovery and decay (Extended Data Fig. 6d).

Consistent with COIN model predictions, participants showed a strong evoked recovery (Fig. 2e). This recovery lasted for the duration of the experiment, defying models that predict a simple exponential decay to the baseline^{4,11,16} (Extended Data Fig. 6e and Extended Data Table 1). We fit the COIN and dual-rate models to the data of individual participants in both experiments (Fig. 2c, e). The COIN model fit the data accurately, but the dual-rate model (and its multi-rate extensions; Extended Data Fig. 6d) showed a qualitative mismatch in the time course of decay of evoked recovery (Fig. 2c, e, insets). Model comparison provided strong support for the COIN model (Δ group-level Bayesian information criterion, BIC, of 302.6 and 394.1 nats for the spontaneous and evoked recovery groups, respectively) and for the majority of participants (6 out of 8 for each experiment; individual fits are shown in Extended Data Fig. 6f).

The COIN model explains memory recovery by creating a new memory only when existing memories cannot account for a perturbation, such as on the abrupt introduction of P^+ and P^- , but not when a new perturbation is introduced gradually. This also explains why de-adaptation is slower after the removal of a gradually (versus abruptly) introduced perturbation¹⁷ (Extended Data Fig. 5p–s).

Contextual inference in memory updating

In the COIN model, contextual inference also controls how each existing memory is updated, that is, proper learning (Fig. 1b). Specifically, all memories are updated, with the updates scaled by their respective inferred responsibilities (Fig. 1h). This contrasts with models that update only a single memory^{11,12} or update multiple memories independent of context^{1,18}. To test this prediction, we examined the extent to which memories for two contexts were updated when we modulated their responsibilities by controlling the sensory cue and state feedback—the two observations that determine context responsibilities (Fig. 1b).

In many scenarios, sensory cues and state feedback provide consistent evidence about context (for example, larger cups are heavier) and, therefore, context responsibilities are approximately all-or-none (Fig. 1h). Thus, to test for graded memory updating, we created conflicts between cues and state feedback (similar to a light, large cup). Specifically, participants experienced an extensive training phase designed to form separate memories for two contexts associated with a distinct cue (target location) and perturbation (Fig. 3a; context 1, P_1^+ ; and context 2, P_2^- , where the subscript and superscript symbols specify the sensory cue and perturbation sign, respectively). These contexts switched randomly (with a probability of 0.5; Fig. 3b). As expected¹⁹, participants formed separate memories for each context and expressed them appropriately based on the sensory cues (Extended Data Fig. 7a). In a subsequent test phase, we studied the updating of one of the memories, the one associated with context 1, in response to exposure to a single trial of a potentially conflicting cue–feedback combination. To quantify single-trial learning for the memory associated with context 1, we assessed the adaptation of this memory using channel trials with the appropriate cue (cue 1) before and after an exposure trial (Fig. 3c). The change in adaptation from the first to the last channel trial of this triplet (channel–exposure–channel) reflects single-trial learning in response to the exposure trial^{4,5}. To bring adaptation close to baseline before each triplet, we used sequences of washout trials, pairing P^0 with the sensory cues (P_1^0 and P_2^0).

The COIN model predicted that the responsibility of context 1 and, therefore, the updating of the corresponding memory (as reflected in single-trial learning; right column in Fig. 3d, Extended Data Fig. 4c) should exhibit a graded pattern that arises over training (Extended Data Fig. 7b)—it should be greatest when the cue and state feedback on the

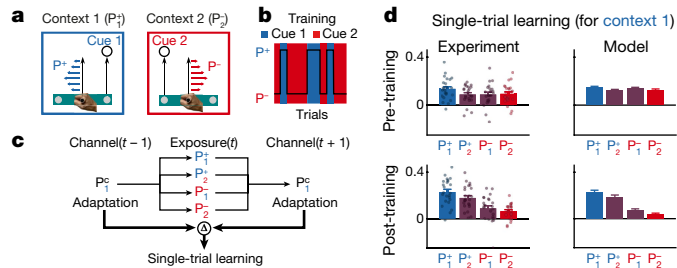


Fig. 3 | Memory updating depends on contextual inference. **a**, Participants experienced two contexts defined by a sensory cue (right or left target) paired with a perturbation sign (P^+ or P^-). Participants moved a control point (right versus left, grey disk) on a virtual bar to the corresponding target¹⁹. For clarity, the schematic is not to scale. The colours of cues and perturbations indicate the context with which they are associated (blue and red for context 1 and 2, respectively). **b**, Training: cues (background colour) were consistently paired with perturbations (black line) randomly selected on each trial (only a few trials are shown for clarity). **c**, Triplets: two channel trials (both with cue 1, P_1^+) bracket an ‘exposure’ trial that uses one of the four possible cue–perturbation combinations. Single-trial learning for the memory associated with context 1 is measured as the difference (Δ) in adaptation across the two channel trials. **d**, Single-trial learning for context 1 before (top) and after (bottom) training. Experimental data (mean \pm s.e.m., left column) for $n = 24$ participants (dots). Positive values indicate single-trial learning consistent with the exposure trial perturbation (increase after P^+ and decrease after P^-). Model data (mean \pm s.e.m., right column) across $n = 24$ fits of the COIN model to individual participants (8 parameters each; Extended Data Fig. 3).

exposure trial both provide evidence of context 1 (P_1^+), least when both provide evidence for context 2 (P_2^-) and intermediate when the two sources of evidence are in conflict (P_2^+ and P_1^- ; see Extended Data Fig. 7c, d and the Supplementary Information for an analytical approximation). Comparing the two conditions with intermediate updating, due to the cues being paired with P^0 in the washout trials, we also expected the cue to have a weaker effect than the perturbation and therefore less updating of the memory for context 1 after exposure with P_1^- than with P_2^+ .

The pattern of single-trial learning in pre- and post-training confirmed the predictions of the COIN model (left column in Fig. 3d). Before training, there was no significant difference in single-trial learning across exposure conditions (two-way repeated-measures ANOVA for cue: $F_{1,23} = 2.40, P = 0.135$; for perturbation: $F_{1,23} = 0.97, P = 0.335$). After learning, single-trial learning showed a gradation across conditions with a significant modulatory effect for both the cue and the perturbation (for cue: $F_{1,23} = 10.35, P = 3.82 \times 10^{-3}$; for perturbation: $F_{1,23} = 21.16, P = 1.26 \times 10^{-4}$; no significant interaction: $F_{1,23} = 0.64, P = 0.432$; Extended Data Fig. 7e). The modulatory effects of the cue and the perturbation were not confined to separate subsets of participants (Fisher’s exact test, odds ratio = 1.0, $P = 1.00$; Methods and Extended Data Fig. 7f). The COIN model also accounted for how single-trial learning changed during the training phase (Extended Data Fig. 7b). Taken together, the pattern of single-trial learning shows the gradation in memory updating (at the individual-participant level) predicted by the COIN model, with multiple memories updated in proportion to their responsibilities.

Apparent changes in learning rate

The COIN model also suggested an alternative account of various classical results about apparent changes in learning rate. Figure 4 shows three paradigms (column 1) with experimental data (column 2). What is common in all these cases is that the empirical finding of trial-to-trial changes in adaptation has been interpreted as proper learning, that is, changes to existing memories (states). Thus, differences between the magnitudes of these changes have been interpreted as differences in learning rate.

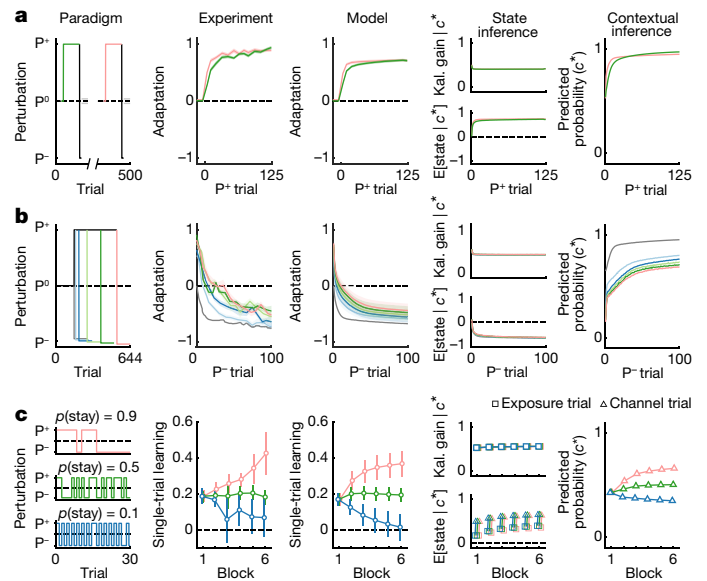


Fig. 4 | Contextual inference underlies apparent changes in learning rate. **a–c**, The COIN model applied to savings (**a**), anterograde interference (**b**) and the effect of environmental consistency on single-trial learning (**c**). Column 1, experimental paradigms (lines as described in Fig. 2b, d, top left; the colours highlight key comparisons). Note that the lines showing P^- perturbations in **b** have been separated vertically for clarity. In **c**, $p(\text{stay})$ is the probability of the perturbation staying the same on the next trial (that is, the self-transition probability). Column 2, experimental data replotted from ref. ²⁰ (**a**), ref. ³ (**b**) and ref. ⁴ (**c**). Column 3, output of COIN model averaged over 40 parameter sets obtained from fits to individual participants in the experiments shown in Figs. 2 and 3 (7 parameters; Extended Data Fig. 3). Model data are mean \pm s.e.m. based on the number of participants in the original experiments; **a**, $n = 46$; **b**, $n = 14$ (light blue), $n = 9$ (other colours, no error bars for the grey condition as they were not shown in the original publication); **c**, $n = 9$ per condition. Columns 4 and 5, COIN model inferences with regard to the context (c^*) that is most relevant to the perturbation to which adaptation is measured. Specifically, c^* is the context with the highest responsibility on the given trial (that associated with P^+ in **a** and P^- in **b**) or, as in Fig. 3d (also single-trial learning), the context with the highest predicted probability on the second channel trial of a triplet (that associated with P^- ; **c**). Column 4, the Kalman gain (Kal. gain) and mean of the predicted state distribution (E[$\text{state} | c^*$]) denotes expected value, bottom) for the relevant context c^* . Column 5, the predicted probability of the relevant context c^* . The grey lines in **b** represent initial adaptation to P^+ and have been sign-inverted in columns 2 and 3 and the bottom panel of column 4. The data in **c** show the averages within blocks, with the bottom panel in column 4 showing separate averages for exposure (squares) and the subsequent channel trials (triangles).

For example, savings (Fig. 4a) refers to the phenomenon that learning the same perturbation a second time (even after washout) is faster than the first time^{1,2,20,21}. In anterograde interference (Fig. 4b), learning a perturbation (P^-) is slower if an opposite perturbation (P^+) has been learned previously, with the amount of interference increasing with the length of experience of the first perturbation³. The persistence of the environment has also been shown to affect single-trial learning (Fig. 4c)—more consistent environments lead to increased levels of single-trial learning^{4,5}.

The COIN model suggests that changes in adaptation can occur without proper learning, simply through apparent learning, that is, by changing the way existing memories are expressed (Fig. 1d–f, blue versus cyan arrows). Thus, apparent changes in learning rate in these paradigms may be due to changes in memory expression rather than changes in memory updating. To test this hypothesis, we simulated the COIN model using the parameters obtained by fitting each of the 40 participants in our experiments (Extended Data Fig. 3). These parameter-free predictions also provided a strong test of the COIN model. The COIN model passed this test: it accurately reproduced the pattern of adaptation and single-trial

learning seen in these paradigms (column 3 in Fig. 4 and Extended Data Fig. 8; Extended Data Fig. 4d–f). Crucially, differences in adaptation and single-trial learning were not driven by differences in either the proper learning rate (Kalman gain; Methods) or the underlying state (column 4 in Fig. 4 and Extended Data Fig. 8). Instead, as hypothesized, they were driven by changes in contextual inference (column 5 in Fig. 4 and Extended Data Fig. 8). For example, according to the COIN model, in savings, P^+ is expected with higher probability during the second exposure after having experienced it during the first exposure. Similarly, anterograde interference arises as more extended experience with P^+ makes it less probable that a transition to other contexts (that is, P^+) will occur. Finally, more (less) consistent environments lead to higher (lower) probabilities with which contexts are predicted to persist to the next trial, leading to more (less) memory expression, as reflected in single-trial learning. Moreover, for single-trial learning, our mathematical analysis indicated that single-trial learning can be expressed mathematically as a mixture of two processes that both depend on contextual inference (Extended Data Fig. 7c, d and Supplementary Information) and each of which can be dissected by the appropriate experimental manipulation—proper learning (as studied in Fig. 3) and apparent learning (as studied in Fig. 4c).

Cognitive mechanisms in the COIN model

The COIN model suggests how specific cognitive mechanisms contribute to the underlying computations. For example, associating working memory with the maintenance of the currently estimated context probabilities explains how a working memory task can effectively lead to evoked recovery in a modified version of the spontaneous recovery paradigm²² (Extended Data Fig. 9a–d and Supplementary Information). Furthermore, identifying explicit and implicit forms of visuomotor learning with inferences in the model about state (that is, estimate of visuomotor rotation) versus a bias parameter (that is, sensory recalibration between the proprioceptive and visual locations of the hand), respectively, explains the complex time courses of these components of learning^{23–25} (Extended Data Fig. 9e–l and Supplementary Information).

Discussion

The COIN model puts the problem of learning a repertoire of memories—rather than a single motor memory—centre stage. Once this more general problem is considered, contextual inference becomes a key computation that unifies seemingly disparate datasets. By partitioning motor learning into two fundamentally different processes, contextual inference (Fig. 1b, top row) and state inference (Fig. 1b, bottom rows), the COIN model provides a principled framework for studying the neural bases of learning motor repertoires (Supplementary Information).

Previous theories of motor learning typically lacked a notion of context^{1,4,18}. In the few cases in which contextual motor learning was considered within a principled probabilistic framework^{11,16,26}, the generative models underlying learning did not incorporate fundamental properties of the environment (such as context transitions, cues or state dynamics) that are critical for explaining a number of learning phenomena. Consequently, previous models can account for only a subset of the datasets that we modelled (Extended Data Table 1), which they were often hand-tailored to address.

There are deep analogies between the context dependence of learning in the motor system and other learning systems, both in terms of their phenomenologies and the computational problems they are trying to solve^{12,27–30}. However, there is one important conceptual issue that has been absent from work on contextual learning in other domains that our research has brought to the fore—the distinction between proper learning and apparent learning. We have shown that many features of motor learning arise not from the updating of existing memories (proper learning) but from changes in the extent to which existing memories are expressed (apparent learning). This distinction, and the role of contextual inference in both proper and apparent learning, is likely to be relevant

to all forms of learning in which experience can be usefully broken down into discrete contexts in the motor system and beyond.

Online content

Any methods, additional references, Nature Research reporting summaries, source data, extended data, supplementary information, acknowledgements, peer review information; details of author contributions and competing interests; and statements of data and code availability are available at <https://doi.org/10.1038/s41586-021-04129-3>.

- Smith, M. A., Ghazizadeh, A. & Shadmehr, R. Interacting adaptive processes with different timescales underlie short-term motor learning. *PLoS Biol.* **4**, e179 (2006).
- Kitago, T., Ryan, S., Mazzoni, P., Krakauer, J. W. & Haith, A. M. Unlearning versus savings in visuomotor adaptation: comparing effects of washout, passage of time, and removal of errors on motor memory. *Front. Hum. Neurosci.* **7**, 307 (2013).
- Sing, G. C. & Smith, M. A. Reduction in learning rates associated with anterograde interference results from interactions between different timescales in motor adaptation. *PLoS Comput. Biol.* **6**, e1000893 (2010).
- Herzfeld, D. J., Vaswani, P. A., Marko, M. K. & Shadmehr, R. A memory of errors in sensorimotor learning. *Science* **345**, 1349–1353 (2014).
- Gonzalez Castro, L. N., Hadjiosif, A. M., Hemphill, M. A. & Smith, M. A. Environmental consistency determines the rate of motor adaptation. *Curr. Biol.* **24**, 1050–1061 (2014).
- McDougle, S. D. et al. Credit assignment in movement-dependent reinforcement learning. *Proc. Natl Acad. Sci. USA* **113**, 6797–6802 (2016).
- Donchin, O., Francis, J. T. & Shadmehr, R. Quantifying generalization from trial-by-trial behavior of adaptive systems that learn with basis functions: theory and experiments in human motor control. *J. Neurosci.* **23**, 9032–9045 (2003).
- Thoroughman, K. A. & Shadmehr, R. Learning of action through adaptive combination of motor primitives. *Nature* **407**, 742–747 (2000).
- Shadmehr, R., Smith, M. A. & Krakauer, J. W. Error correction, sensory prediction, and adaptation in motor control. *Annu. Rev. Neurosci.* **33**, 89–108 (2010).
- Wolpert, D. M. & Kawato, M. Multiple paired forward and inverse models for motor control. *Neural Netw.* **11**, 1317–1329 (1998).
- Oh, Y. & Schweighofer, N. Minimizing precision-weighted sensory prediction errors via memory formation and switching in motor adaptation. *J. Neurosci.* **39**, 9237–9250 (2019).
- Gershman, S. J., Radulescu, A., Norman, K. A. & Niv, Y. Statistical computations underlying the dynamics of memory updating. *PLoS Comput. Biol.* **10**, e1003939 (2014).
- Hulst, T. et al. Cerebellar degeneration reduces memory resilience after extended training. Preprint at *bioRxiv* <https://doi.org/10.1101/2020.07.03.185959> (2021).
- Pekny, S. E., Criscimagna-Hemminger, S. E. & Shadmehr, R. Protection and expression of human motor memories. *J. Neurosci.* **31**, 13829–13839 (2011).
- Rescorla, R. A. & Heth, C. D. Reinstatement of fear to an extinguished conditioned stimulus. *J. Exp. Psychol. Anim. Behav. Process.* **1**, 88–96 (1975).
- Berniker, M. & Kording, K. Estimating the sources of motor errors for adaptation and generalization. *Nat. Neurosci.* **11**, 1454–1461 (2008).
- Taylor, J. A., Wojaczynski, G. J. & Ivry, R. B. Trial-by-trial analysis of intermanual transfer during visuomotor adaptation. *J. Neurophysiol.* **106**, 3157–3172 (2011).
- Kording, K. P., Tenenbaum, J. B. & Shadmehr, R. The dynamics of memory as a consequence of optimal adaptation to a changing body. *Nat. Neurosci.* **10**, 779–786 (2007).
- Heald, J. B., Ingram, J. N., Flanagan, J. R. & Wolpert, D. M. Multiple motor memories are learned to control different points on a tool. *Nat. Hum. Behav.* **2**, 300–311 (2018).
- Coltman, S. K., Cashaback, J. G. A. & Gribble, P. L. Both fast and slow learning processes contribute to savings following sensorimotor adaptation. *J. Neurophysiol.* **121**, 1575–1583 (2019).
- Huang, V. S., Haith, A., Mazzoni, P. & Krakauer, J. W. Rethinking motor learning and savings in adaptation paradigms: model-free memory for successful actions combines with internal models. *Neuron* **70**, 787–801 (2011).
- Keisler, A. & Shadmehr, R. A shared resource between declarative memory and motor memory. *J. Neurosci.* **30**, 14817–14823 (2010).
- McDougle, S. D., Ivry, R. B. & Taylor, J. A. Taking aim at the cognitive side of learning in sensorimotor adaptation tasks. *Trends Cogn. Sci.* **20**, 535–544 (2016).
- McDougle, S. D., Bond, K. M. & Taylor, J. A. Explicit and implicit processes constitute the fast and slow processes of sensorimotor learning. *J. Neurosci.* **35**, 9568–9579 (2015).
- Miyamoto, Y. R., Wang, S. & Smith, M. A. Implicit adaptation compensates for erratic explicit strategy in human motor learning. *Nat. Neurosci.* **23**, 443–455 (2020).
- Haruno, M., Wolpert, D. M. & Kawato, M. MOSAIC model for sensorimotor learning and control. *Neural Comput.* **13**, 2201–2220 (2001).
- Gershman, S. J., Blei, D. M. & Niv, Y. Context, learning, and extinction. *Psychol. Rev.* **117**, 197–209 (2010).
- Sanders, H., Wilson, M. A. & Gershman, S. J. Hippocampal remapping as hidden state inference. *eLife* **9**, e51140 (2020).
- Collins, A. & Koehlin, E. Reasoning, learning, and creativity: frontal lobe function and human decision-making. *PLoS Biol.* **10**, e1001293 (2012).
- Collins, A. G. E. & Frank, M. J. Cognitive control over learning: creating, clustering, and generalizing task-set structure. *Psychol. Rev.* **120**, 190–229 (2013).

Publisher's note Springer Nature remains neutral with regard to jurisdictional claims in published maps and institutional affiliations.

© The Author(s), under exclusive licence to Springer Nature Limited 2021

Methods

Here we provide an overview of the methods. Full details are provided in the Supplementary Information.

Participants

Forty right-handed, neurotypical participants (18 males and 22 females; aged 27.7 ± 5.6 years, mean \pm s.d.) participated in two experiments, which were approved by the Cambridge Psychology Research Ethics Committee and the Columbia University IRB (AAAR9148). All of the participants provided written informed consent.

Experimental apparatus

Experiments were performed using a vBOT planar robotic manipulandum with a virtual-reality system and air table³¹. Participants grasped the handle of the manipulandum with their right hand while their forearm was supported on an air sled and moved their hand in the horizontal plane.

The manipulandum controlled a virtual ‘object’ that was displayed centred on the hand and translated with hand movements as the participants made repeated movements from a home position to a target located 12 cm distally in the sagittal direction.

On each trial, the vBOT could either generate no forces (P^0 , null field), a velocity-dependent curl force field (P^+ or P^- perturbation depending on the direction of the field) or a force channel (P^c , channel trials). For the curl force field, the force generated on the hand was given by

$$\begin{bmatrix} F_x \\ F_y \end{bmatrix} = g \begin{bmatrix} 0 & -1 \\ 1 & 0 \end{bmatrix} \begin{bmatrix} \dot{x} \\ \dot{y} \end{bmatrix} \quad (1)$$

where F_x , F_y , \dot{x} and \dot{y} are the forces and velocities at the handle in the x (transverse) and y (sagittal) directions, respectively. The gain, g , was set to $\pm 15 \text{ N s m}^{-1}$, with the sign specifying the direction of the curl field (counterclockwise or clockwise, which were assigned to P^+ and P^- , counterbalanced across participants). During the channel trials, the hand was constrained to move along a straight line to the target by simulating channel walls on each side of the straight line as stiff springs ($3,000 \text{ N m}^{-1}$) with damping (140 N s m^{-1})^{32,33}.

Experiment 1: spontaneous and evoked recovery

Sixteen participants were randomly assigned to either a spontaneous ($n = 8$) or evoked ($n = 8$) recovery group. The virtual object controlled by participants was simply a cursor.

The participants in the spontaneous recovery group performed a version of the standard spontaneous recovery paradigm¹. A pre-exposure phase (50 trials) with a null field (P^0) was followed by an exposure phase (125 trials) with P^+ . The participants then underwent a counter-exposure phase (15 trials) with the opposite perturbation (P^-). This was followed by a channel-trial phase (150 channel trials, P^c). In the pre-exposure and exposure phases, to assess adaptation, each block of 10 trials had one channel trial (P^c) in a random location (not the first). A 45 s rest break was given after trial 60 of the exposure phase, followed by an additional 5 P^+ trials prepended to the next block.

The evoked recovery group experienced the identical paradigm to the spontaneous recovery group except that the third and fourth trials of the channel-trial phase were replaced with P^+ trials (Fig. 2d).

Experiment 2: memory updating

Twenty-four participants performed the memory updating experiment. The paradigm is based on the control point experiment described in ref.¹⁹ in which perturbations P^0 , P^+ and P^- are presented with one of two possible sensory cues (different control points on a rectangular virtual object). The experiment consisted of a pre-training, training and post-training phase. In the pre-training and post-training phases, participants performed blocks of trials consisting of a variable number

(8, 10 or 12 in the pre-training phase, and 2, 4 or 6 in the post-training phase) of washout trials (an equal number of P_1^0 and P_2^0 in a pseudorandom order, where the subscript values denote cues) followed by 1 of 4 possible ‘triplets’. Each triplet consisted of 2 channel trials (both with cue 1, P_1^+) bracketing a cue–perturbation ‘exposure’ trial (P_1^+ , P_2^+ , P_1^- or P_2^- , see the main text and Fig. 3c). Each of the 4 triplet types was experienced once every 4 blocks, using pseudorandom permutations, with a total of 16 blocks in the pre-training phase and 32 blocks in the post-training phase.

In the training phase (Fig. 3b), the participants performed 24 blocks each consisting of 62–70 trials. The key feature of each block was that 32 force-field trials (equal number of P_1^+ and P_2^+ in a pseudorandom order) was followed by 2 triplets (with exposure trials of P_1^+ and P_2^+). Each triplet was preceded by a variable number of washout trials (equal number of P_1^0 and P_2^0 in a pseudorandom order) to bring adaptation back close to baseline. Full details of the block structure are provided in the Supplementary Information.

The control point assigned to sensory cue 1 (used on all triplet channel trials) and sensory cue 2 was counterbalanced across participants, as was the direction of force field assigned to P^+ and P^- . Note that counterbalancing the sensory cues and force field directions across participants guarantees that the results we obtained would have had the opposite pattern (greatest single-trial learning for P_2^- and least for P_1^+ ; compare with Fig. 3d, bottom left) had we probed the memory for context 2 (using P_2^c channel trials). Thus, this design allows us to draw conclusions about multiple memories being updated simultaneously, while measuring the updating of only one memory for each participant.

Data analysis

On each channel trial, we linearly regressed the time series of actual forces generated by participants into the channel wall against the ideal forces that would fully compensate for the forces on a force-field trial¹. The offset of the regression was constrained to zero, and we used the slope as our (dimensionless) measure of adaptation.

To identify changes in single-trial learning between triplets in the memory updating experiment, two-way repeated-measures ANOVAs were performed with factors of cue (2 levels: cue 1 and cue 2) and perturbation (2 levels: P^+ and P^-). To test whether the modulatory effects of cue and perturbation were confined to separate subsets of the participants, we quantified the effect of each by computing, on an individual-participant basis, the following contrasts in single-trial learning: $P_1^+ + P_1^- - P_2^+ - P_2^-$ (cue effect) and $P_1^+ + P_2^+ - P_1^- - P_2^-$ (perturbation effect). We then split participants into 2×2 groups on the basis of whether each effect was below or above the median of each effect and performed a Fisher’s exact test on the resulting 2×2 histogram (Supplementary Information).

All statistical tests were two-sided with significance set to $P < 0.05$. Data analysis was performed using MATLAB R2020a.

COIN generative model

Figure 1a shows the graphical model for the generative model. At each time step $t = 1, \dots, T$, there is a discrete latent variable (the context) $c_t \in \{1, \dots, \infty\}$ that evolves as a Markov process:

$$c_t | c_{t-1}, \Pi \sim \text{Discrete}(\boldsymbol{\pi}_{c_{t-1}}), \quad (2)$$

where $\Pi = (\boldsymbol{\pi}_j)_{j=1}^{\infty}$ is the transition probability matrix and $\boldsymbol{\pi}_j = (\pi_{jk})_{k=1}^{\infty}$ is its j th row containing the transition probabilities from context j to each context k (including itself). In principle, there are an infinite number of rows and columns in this matrix. However, in practice, generation and inference can both be accomplished using finite-sized matrices by placing a nonparametric prior on the matrix (see below).

Each context j is associated with a continuous (scalar) latent variable $x_t^{(j)}$ (the state, for example, the strength of a force field) that evolves

according to its own linear-Gaussian dynamics independently of all other states:

$$x_t^{(j)} = a^{(j)} x_{t-1}^{(j)} + d^{(j)} + w_t^{(j)} \quad w_t^{(j)} \sim \mathcal{N}(0, \sigma_q^2), \quad (3)$$

where $a^{(j)}$ and $d^{(j)}$ are the context-specific state retention factor and drift, respectively, and σ_q^2 is the variance of the process noise (shared across contexts). Each state is assumed to have existed for long enough that its prior for the first time it is observed is its stationary distribution:

$$\lim_{t \rightarrow \infty} x_t^{(j)} \sim \mathcal{N}\left(\frac{d^{(j)}}{1-a^{(j)}}, \frac{\sigma_q^2}{1-[a^{(j)}]^2}\right). \quad (4)$$

At each time step, a continuous (scalar) observation y_t (the state feedback) is emitted from the state associated with the current context:

$$y_t = x_t^{(c_t)} + v_t \quad v_t \sim \mathcal{N}(0, \sigma_r^2), \quad (5)$$

where σ_r^2 is the variance of the observation noise (also shared across contexts).

In addition to the state feedback, a discrete observation (the sensory cue) $q_t \in \{1, \dots, \infty\}$ is also emitted. The distribution of sensory cues depends on the current context:

$$q_t | c_t, \Phi \sim \text{Discrete}(\Phi_{c_t}), \quad (6)$$

where $\Phi = (\Phi_j)_{j=1}^{\infty}$ is the cue probability matrix (which, in principle, is also doubly infinite in size but can be treated as finite in practice) and $\Phi_j = (\Phi_{jk})_{k=1}^{\infty}$ is its j th row containing the probability of each cue k in context j .

To make this infinite-dimensional switching state-space model well defined, we place hierarchical Dirichlet process priors³⁴ on the transition and cue probability matrices. The transition probability matrix is generated in two steps (Extended Data Fig. 1a). First, an infinite set of global probabilities for transitioning into each context $\beta = (\beta_j)_{j=1}^{\infty}$ ('global transition probabilities') is generated by sampling from a Griffiths, Engen and McCloskey (GEM) distribution:

$$\beta | \gamma \sim \text{GEM}(\gamma), \quad (7)$$

where $0 \leq \beta_j \leq 1$ and $\sum_{j=1}^{\infty} \beta_j = 1$, as required for a set of probabilities. The global transition probabilities decay exponentially as a function of j in expectation, with the hyperparameter γ controlling the rate of decay and thus the effective number of contexts: a large γ implies a large number of small-probability contexts (slow decay from a relatively small initial probability), whereas a small γ implies a smaller number of relatively large-probability contexts (fast decay from a relatively large initial probability).

Second, for each context (row of the transition probability matrix), an infinite set of local (context-specific) probabilities for transitioning into each context $\pi_j = (\pi_{jk})_{k=1}^{\infty}$ ('local transition probabilities') are generated via a 'sticky' variant³⁵ of the Dirichlet process (DP):

$$\pi_j | \alpha, \beta, \kappa \sim \text{DP}\left(\alpha + \kappa, \frac{\alpha \beta + \kappa \delta_j}{\alpha + \kappa}\right), \quad (8)$$

where $0 \leq \pi_{jk} \leq 1$ and $\sum_{k=1}^{\infty} \pi_{jk} = 1$, as required for a set of probabilities, and δ_j is an infinite-dimensional one-hot vector with the j th element set to 1 and all other elements set to 0. The mean (base) distribution of the Dirichlet process is $(\alpha \beta + \kappa \delta_j) / (\alpha + \kappa)$, with large $\alpha + \kappa$ reducing variability around this mean (for a tutorial on the Dirichlet process, see ref.³⁶). Thus, the concentration parameter α controls the resemblance of local transition probabilities to the global transition

probabilities β . The self-transition bias parameter $\kappa > 0$ controls the resemblance of local transition probabilities to δ_j (that is, a certain self-transition, $c_t = c_{t-1} = j$). This self-transition bias expresses the fact that a context often persists for several time steps before switching (that is, that contexts are sticky), such as when an object is manipulated for an extended period of time.

Note that the rows of the transition probability matrix are dependent as their expected values (the base distributions of the corresponding Dirichlet processes) contain a shared term, the global transition distribution β . This dependency, controlled by α , captures the intuitive notion that contexts that are common in general (that is, have a large global transition probability) will be transitioned to frequently from all contexts.

The cue probability matrix $\Phi = (\Phi_j)_{j=1}^{\infty}$ is generated using an analogous (non-sticky) hierarchical construction:

$$\beta^e | \gamma^e \sim \text{GEM}(\gamma^e) \quad \Phi_j | \alpha^e, \beta^e \sim \text{DP}(\alpha^e, \beta^e), \quad (9)$$

where γ^e determines the distribution of the global cue probabilities β^e and α^e determines the across-context variability of local cue probabilities around the global cue probabilities.

To allow full Bayesian inference over the parameters governing the state dynamics $\omega^{(j)} = [a^{(j)}, d^{(j)}]^T$, we also place a prior on these parameters. For this, we use a bivariate normal distribution (truncated between 0 and 1 for $a^{(j)}$):

$$\omega^{(j)} | \mu, \Sigma \sim \mathcal{TN}(\mu, \Sigma), \quad (10)$$

where $\mu = [\mu_a, 0]^T$ and $\Sigma = \text{diag}(\sigma_a^2, \sigma_d^2)$ is a diagonal covariance matrix. Here we have set the prior mean of $d^{(j)}$ to zero under the assumption that positive and negative drifts are equally probable.

Inference in the COIN model

At each time step $t = 1, \dots, T$, the goal of inference is to compute the joint posterior distribution $p(\Theta_t | y_{1:t}, q_{1:t})$ of all quantities $\Theta_t = \{c_t, \{x_t^{(j)}, \omega^{(j)}\}_{j=1}^{\infty}, \beta, \Pi, \beta^e, \Phi\}$ that are not directly observed by the learner: the current context c_t , the current state of each context $x_t^{(j)}$, the parameters governing the state dynamics in each context $\omega^{(j)}$, the context transition parameters (global β and local Π transition probabilities) and the cue emission parameters (global β^e and local Φ cue probabilities) based on the sequence of state feedback $y_{1:t}$ and sensory cue observations $q_{1:t}$, made until time t and t' , respectively (with t and t' each being either t or $t-1$; see below). In principle, this posterior is fully determined by the generative model that was defined in the previous section and can be obtained in a sequential manner by recursively propagating (filtering) the joint posterior from one time point to the next after each new set of observations is made. As exact inference is infeasible, we use a sequential Monte Carlo method known as particle learning that computes an approximation to this filtered posterior^{37,38}. We extensively validated the accuracy of this method (Extended Data Fig. 2a, b). The details of the inference method are provided in the Supplementary Information. Here we describe only how the approximate posterior is used to obtain the main model-derived quantities plotted in the paper.

The predicted probability of context $j \in \{1, \dots, J, \emptyset\}$, where j is the number of known contexts and \emptyset is the novel context, on trial t (computed after observing the cue but before observing the state feedback; Fig. 1f, Fig. 2b, d, top right and column 5 in Fig. 4a–c) is

$$p(c_t = j | q_t, \dots) = \int p(c_t = j, \Theta_t \setminus c_t | q_t, \dots) d\Theta_t \setminus c_t, \quad (11)$$

where $\Theta_t \setminus c_t$ denotes the set Θ_t excluding c_t and \dots represents all of the observations before time t (as in Fig. 1). The responsibility of context j on trial t (computed after observing both the cue and the state feedback; Fig. 1g, h) is

$$p(c_t=j|q_t, y_t, \dots) = \int p(c_t=j, \theta_t \setminus c_t | q_t, y_t, \dots) d\theta_t \setminus c_t. \quad (12)$$

The predicted state distribution for context j on trial t (computed before observing the state feedback; Fig. 1d and Fig. 2b,d, bottom left) is

$$p(x_t^{(j)}|\dots) = \int p(x_t^{(j)}, \theta_t \setminus x_t^{(j)}|\dots) d\theta_t \setminus x_t^{(j)}, \quad (13)$$

where $\theta_t \setminus x_t^{(j)}$ denotes the set θ_t excluding $x_t^{(j)}$. The mean of this distribution $\hat{x}_t^{(j)}$ (bottom of column 4 in Fig. 4a–c) can be shown to evolve across trials (Supplementary Information) as

$$\hat{x}_{t+1}^{(j)} = \mathbb{E}_{p(a^{(j)}|c_t, q_t, y_t, \dots)}[a^{(j)}](\hat{x}_t^{(j)} + p(c_t=j|q_t, y_t, \dots)k_t^{(j)}e_t^{(j)}) + \mathbb{E}_{p(a^{(j)}|c_t, q_t, y_t, \dots)}[a^{(j)}], \quad (14)$$

where $\mathbb{E}_{p(a^{(j)}|c_t, q_t, y_t, \dots)}[a^{(j)}]$ denotes the expected value of $a^{(j)}$ with respect to the distribution $p(a^{(j)}|c_t, q_t, y_t, \dots)$, $e_t^{(j)} = y_t - \hat{x}_t^{(j)}$ is the prediction error for context j , and $k_t^{(j)}$ corresponds to the Kalman gain for context j , which we plot in Fig. 4. Note that this update is scaled by the context's responsibility $p(c_t=j|q_t, y_t, \dots)$, which underlies the effect of contextual inference on memory updating (Fig. 1b).

The 'overall' predicted state distribution on trial t (that is, the predicted state distribution of the context that is currently active, and of which the identity the learner cannot know with certainty; purple distribution in Fig. 1e and Fig. 2b, d, bottom right) is computed by integrating out the context from equation (13) using the predicted probabilities from equation (11) (Fig. 1b):

$$\mathbb{E}_{p(c_t|q_t, \dots)}[p(x_t^{(c_t)}|\dots)] = \sum_{j=\{1, \dots, J, \emptyset\}} p(x_t^{(j)}|\dots)p(c_t=j|q_t, \dots). \quad (15)$$

The motor output u_t of the learner (Fig. 1e, cyan line, Fig. 2b, d, bottom right, cyan line and column 3 in Fig. 4a, b) is the mean of this predicted state distribution:

$$u_t = \sum_{j=\{1, \dots, J, \emptyset\}} \hat{x}_t^{(j)} p(c_t=j|q_t, \dots). \quad (16)$$

Applying the COIN model to experimental data

Applying the COIN model to experimental data required solving two additional challenges. First, participants' state feedback observations are hidden from the perspective of the experimenter, as they are noisy realizations of the true underlying states (equation (5)). To appropriately account for our uncertainty about the state feedback participants actually observed, we computed the distribution of COIN model inferences by integrating over the possible sequences of state feedback observations $y_{1:T}$ given the sequence of true states (experimentally applied perturbations) $x_{1:T}^*$ (ref. 39). Specifically, on each trial, x_t^* was assigned a value of 0 (null-field trials), +1 (P^+ perturbation trials) or -1 (P^- perturbation trials) and y_t was assumed to be distributed around x_t^* with independent and identically distributed (i.i.d.) zero-mean Gaussian observation noise of variance σ_y^2 (equation (5)), except on channel trials (P^c) where we treated y_t as unobserved, as the state (the magnitude of a force field) was not observed by the participants on those trials. Note that the distribution of state feedback given the true state $p(y_t|x_t^*)$ shares the same parameters as those underlying the COIN model inferences as it is self-consistently defined by the generative model. All figures showing COIN model inferences applied to experimental data (that is, all but Fig. 1) show the quantities described in the previous section after the state feedback has been integrated out (Fig. 1d–h shows COIN model inferences conditioned on the state feedback sequence shown in Fig. 1c).

Second, the behaviour of real participants can always be subject to influences that are not explicitly included in the COIN model. To

account for these uncontrolled and unmodelled factors, we introduced a phenomenological 'motor noise' component that relates the motor output u_t of the COIN model (equation (16)) to the experimentally measured adaptation a_t via i.i.d. zero-mean Gaussian noise:

$$a_t \sim \mathcal{N}(u_t, \sigma_m^2), \quad (17)$$

where σ_m is the s.d. of the motor noise.

Model fitting and model comparison

In experiments 1 and 2, we fit the parameters of the COIN model ϑ to participants' data by maximizing the data log likelihood using Bayesian adaptive direct search (BADS)⁴⁰. In Experiment 1, $\vartheta = \{\sigma_q, \mu_a, \sigma_a, \sigma_d, \alpha, \rho, \sigma_m\}$, where

$$\rho = \kappa / (\alpha + \kappa) \quad (18)$$

is the normalized self-transition bias parameter. In Experiment 2, which included sensory cues, an additional parameter α^c was also fit. In Experiment 1, we also fit a two-state (dual-rate) and three-state state-space model to the data of individual participants by minimizing the mean squared error using MATLAB's `fmincon` and `BADS`. In all cases, optimization was performed from 30 random initial parameter settings (Supplementary Information).

To perform model comparison for individual participants, we calculated the BIC. A BIC difference of greater than 4.6 nats (a Bayes factor of greater than 10) is considered to provide strong evidence in favour of the model with the lower BIC value⁴¹. To perform a model comparison at the group level, we calculated the group-level BIC, which is the sum of BICs over individuals⁴².

Parameter and model recovery

We used the parameters from the fits of the COIN and dual-rate models to the data of each participant in the spontaneous and evoked recovery experiments to generate ten synthetic datasets per model class (COIN and dual-rate) for each participant from the corresponding experiment. In the dual-rate model, the only source of variability across the different synthetic datasets for a given participant was motor noise. By contrast, for the COIN model, sensory noise provided another source of variability in addition to motor noise. We fit both model classes to each synthetic data set as we did with real data (see above).

For parameter recovery (Extended Data Fig. 2c), we compared the COIN model parameters that were used to generate the synthetic data (true parameters) with the COIN model parameters fit to these synthetic datasets (recovered parameters).

For model recovery (Extended Data Fig. 2d, e), we examined the proportion of times that the difference in BIC between the COIN and dual-rate fits favoured the true model class that generated the data.

Simulating existing datasets

We performed COIN model simulations on a diverse set of extant data in Fig. 4 (similarly Extended Data Figs. 5, 8 and 9) in a purely cross-validated manner, such that we used model parameters fitted to participants in our own experiments to make predictions for experiments conducted in other laboratories using other paradigms.

The paradigms in Fig. 4 and Extended Data Fig. 8 were simulated using the 40 sets of parameters fit to our individual participants' data from both experiments. One hundred simulations (each conditioned on a different noisy state feedback sequence) were performed for each parameter set. The results shown are based on the average of all of these simulations.

The paradigms in Extended Data Figs. 5a–o and 9 were variations of the standard spontaneous recovery paradigm. We therefore simulated these paradigms (as well as the paradigm in Extended Data Fig. 5p–s)

using the parameters fit to the average spontaneous and evoked recovery datasets. One hundred simulations (each conditioned on a different noisy state feedback sequence) were performed. The results shown are based on the average of these simulations.

Modelling working memory

A working memory task performed after the last P⁻ trial of a spontaneous recovery paradigm has been shown to interfere with spontaneous recovery, producing an effect that is reminiscent of evoked recovery on the first P^c trial²² (Extended Data Fig. 9a). We modelled the effect of the working memory task as selectively abolishing the (working) memory of the responsibilities on the last P⁻ trial (Extended Data Fig. 9b–d). This means that, on the first P^c trial, the predicted probabilities are based on the expected context frequencies (the stationary probabilities).

Modelling visuomotor learning and its explicit and implicit components

In visuomotor rotation experiments, the cursor moves in a different direction to the hand (which is occluded from vision). Thus, visuomotor rotations introduce a discrepancy between the location of the hand as sensed by vision and proprioception. To model this discrepancy, we include a context-specific bias parameter $b^{(c)}$ in the state feedback (equation (5)):

$$y_t = x_t^{(c)} + b^{(c)} + v_t \quad v_t \sim \mathcal{N}(0, \sigma_v^2). \quad (19)$$

To support Bayesian inference, we place a normal distribution prior over this parameter:

$$b^{(j)} | \mu_b, \sigma_b \sim \mathcal{N}(\mu_b, \sigma_b^2). \quad (20)$$

We set μ_b to zero based on the assumption that positive and negative biases are equally probable and σ_b to 70^{-1} by hand to match the empirical data in Extended Data Fig. 9e. We extend and modify the inference algorithm accordingly (Supplementary Information).

On each trial, the state feedback was assigned a value of 0 (no rotation trials), +1 (P⁺ rotation trials) or -1 (P⁻ rotation trials) plus i.i.d. zero-mean Gaussian observation noise with variance σ_r^2 . Visual error-clamp trials (P^c) were modelled in the same way as channel trials (that is, with state feedback unobserved). Adaptation was modelled as the mean of the predicted state feedback distribution (Extended Data Figs. 5q and 9f, dashed pink line) plus Gaussian motor noise.

We also modelled an experiment in which an explicit judgement of the perturbation is obtained on every trial, and the implicit component is taken as the difference between adaptation and the explicit judgement²³. We hypothesized that participants have explicit access to the state representing their belief about the visuomotor rotation but do not have access to the bias in the state feedback, which is therefore implicit. Thus, we mapped the state of the context with the highest responsibility on the previous trial (Extended Data Fig. 9h, black line) onto the explicit component and the average bias across contexts weighted by the predicted probabilities (Extended Data Fig. 9j, cyan line) onto the implicit component. Adaptation is then, by definition, the sum of these two components (Extended Data Fig. 9e, solid pink) plus Gaussian motor noise. Full details are provided in the Supplementary Information.

Reporting summary

Further information on research design is available in the Nature Research Reporting Summary linked to this paper.

Data availability

All experimental data are publicly available at the Dryad repository (<https://doi.org/10.5061/dryad.m63xsj42r>). The data include the raw kinematics and force profiles of individual participants on all trials as well as the adaptation measures used to generate the experimental data shown in Figs. 2c, e and 3d.

Code availability

The code for the COIN model is available at GitHub (<https://github.com/jamesheald/COIN>).

- Howard, I. S., Ingram, J. N. & Wolpert, D. M. A modular planar robotic manipulandum with end-point torque control. *J. Neurosci. Methods* **181**, 199–211 (2009).
- Milner, T. E. & Franklin, D. W. Impedance control and internal model use during the initial stage of adaptation to novel dynamics in humans. *J. Physiol.* **567**, 651–664 (2005).
- Scheidt, R. A., Reinkensmeyer, D. J., Conditt, M. A., Rymer, W. Z. & Mussa-Ivaldi, F. A. Persistence of motor adaptation during constrained, multi-joint, arm movements. *J. Neurophysiol.* **84**, 853–862 (2000).
- Teh, Y. W., Jordan, M. I., Beal, M. J. & Blei, D. M. Hierarchical Dirichlet processes. *J. Am. Stat. Assoc.* **101**, 1566–1581 (2006).
- Fox, E. B., Sudderth, E. B., Jordan, M. I. & Willsky, A. S. An HDP-HMM for systems with state persistence. In *Proc. 25th International Conference on Machine Learning* (eds McCallum, A. & Roweis, S.) 312–319 (Omnipress, 2008).
- Teh, Y. W. in *Encyclopedia of Machine Learning* (eds Sammut, C. & Webb, G. I.) 280–287 (Springer, 2011).
- Carvalho, C. M., Johannes, M. S., Lopes, H. F. & Polson, N. G. Particle learning and smoothing. *Stat. Sci.* **25**, 88–106 (2010).
- Lopes, H. F., Carvalho, C. M., Johannes, M. S., & Polson, N. G. in *Bayesian Statistics 9* (eds Bernardo, J. M. et al.) (Oxford Univ. Press, 2011).
- Houlsby, N. et al. Cognitive tomography reveals complex, task-independent mental representations. *Curr. Biol.* **23**, 2169–2175 (2013).
- Acerbi, L. & Ma, W. J. Practical Bayesian optimization for model fitting with Bayesian adaptive direct search. In *Proc. Advances in Neural Information Processing Systems* (eds Guyon, I. et al.) 1836–1846 (Curran, 2017).
- Jeffreys, H. *The Theory of Probability* (Oxford Univ. Press, 1998).
- Li, J., Wang, Z. J., Palmer, S. J. & McKeown, M. J. Dynamic Bayesian network modeling of fMRI: a comparison of group-analysis methods. *Neuroimage* **41**, 398–407 (2008).

Acknowledgements We thank J. N. Ingram for technical support and G. Hennequin for discussions. This work was supported by the European Research Council (ERC) under the European Union's Horizon 2020 research and innovation programme (grant agreement no. 726090 to M.L.), the Wellcome Trust (Investigator Awards 212262/Z/18/Z to M.L. and 097803/Z/11/Z to D.M.W.), the Royal Society (Noreen Murray Professorship in Neurobiology to D.M.W.), the National Institutes of Health (R01NS117699 and U19NS104649 to D.M.W.) and Engineering and Physical Sciences Research Council (studentship to J.B.H.).

Author contributions J.B.H. developed the model, implemented the model, performed the experiments, analysed the data and performed simulations. J.B.H. and D.M.W. designed the behavioural experiments. All of the authors were involved in the conceptualization of the study, developed techniques for analysing the model, interpreted results and wrote the paper.

Competing interests The authors declare no competing interests.

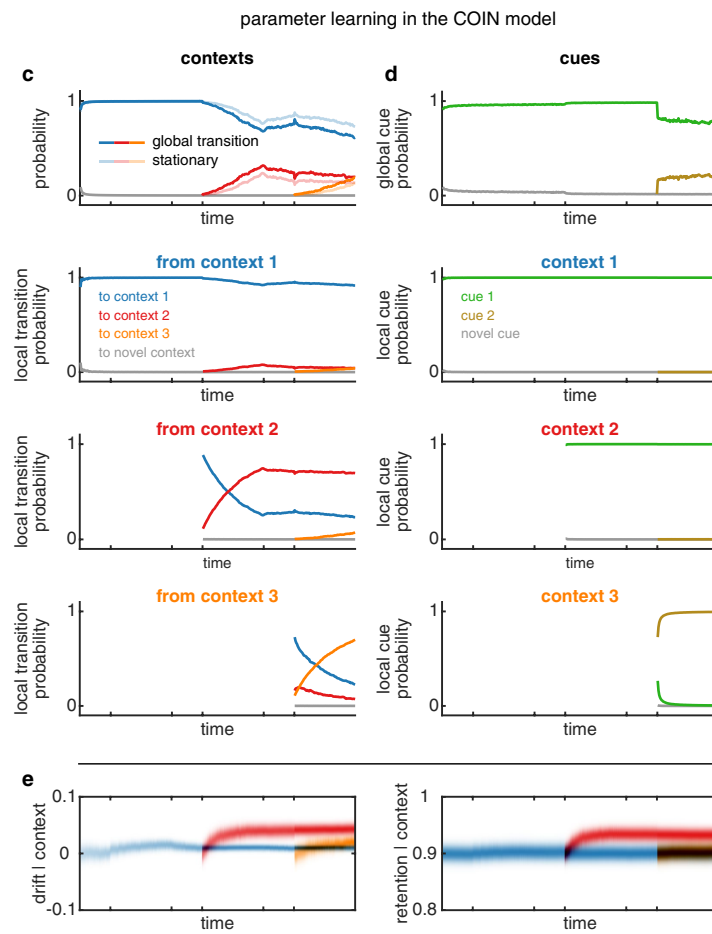
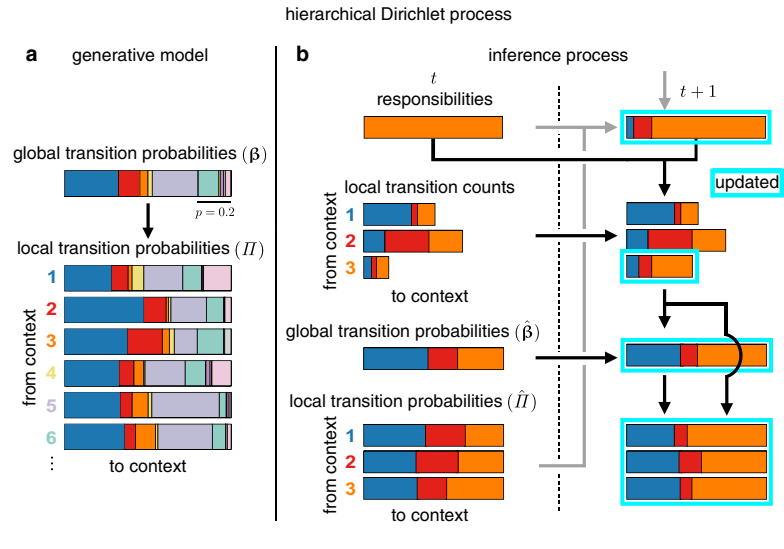
Additional information

Supplementary information The online version contains supplementary material available at <https://doi.org/10.1038/s41586-021-04129-3>.

Correspondence and requests for materials should be addressed to James B. Heald.

Peer review information Nature thanks the anonymous reviewers for their contribution to the peer review of this work. Peer reviewer reports are available.

Reprints and permissions information is available at <http://www.nature.com/reprints>.

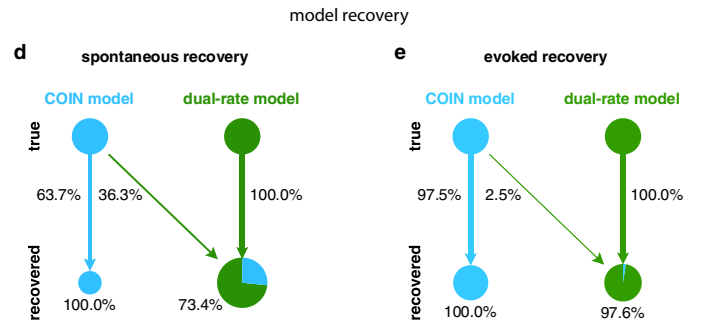
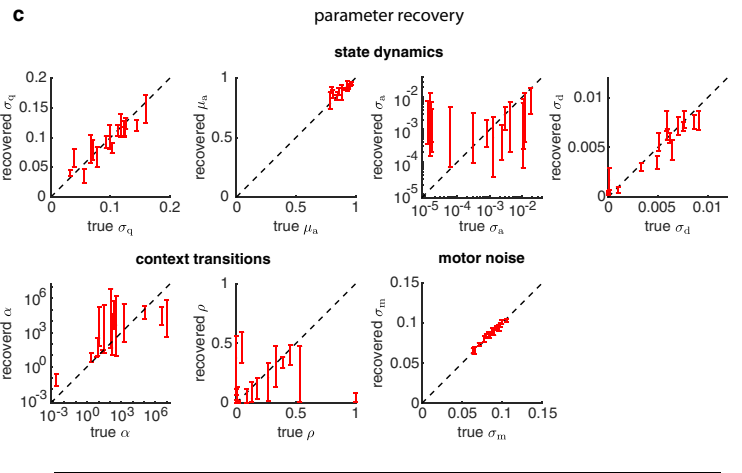
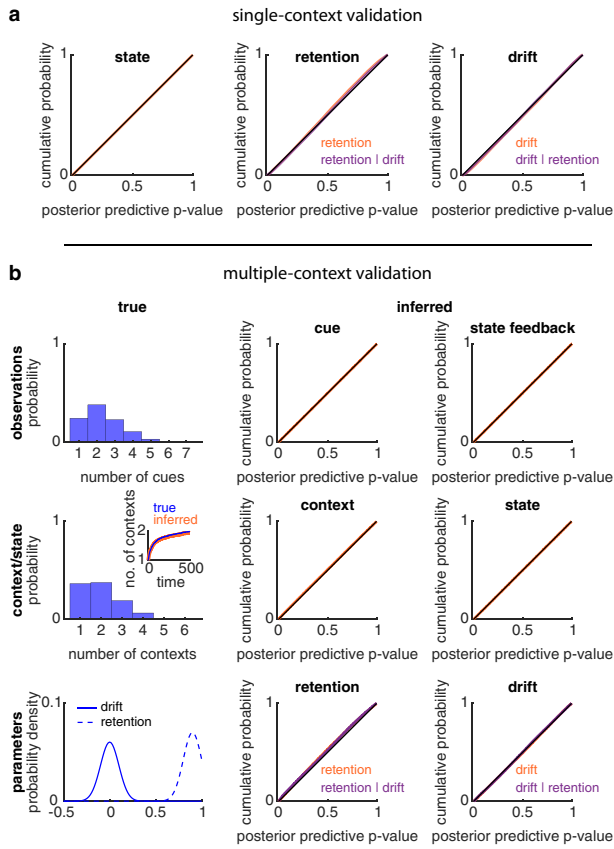


Extended Data Fig. 1 | See next page for caption.

Extended Data Fig. 1 | Additional details of the COIN model (related to Fig. 1). a-b, Hierarchy and generalization in contextual inference. **a**, Local transition probabilities are generated in two steps via a hierarchical Dirichlet process. In the first step (top), an infinite set of global transition probabilities β are generated via a stochastic stick-breaking process (Supplementary Information). Probabilities are represented by the width of bar segments with different colours indicating different contexts. In the second step (bottom), for each context ('from context'), local transition probabilities to each context ('to context') are generated (a row of Π) via a stochastic Dirichlet process and are equal to the global probabilities in expectation (bar a self-transition bias, which we set to zero here for clarity). (An analogous hierarchical Dirichlet process, not shown, is used to generate the global and local cue probabilities.) **b**, Contextual inference updates both the global and local transition probabilities. Context transition counts are maintained for all from-to pairs of known contexts and get updated based on the contexts inferred on two consecutive time points (responsibilities at time points t and $t+1$). These updated context transition counts are used to update the inferred global transition probabilities $\hat{\beta}$. The updated global transition probabilities and context transition counts produce new inferences about the inferred local transition probabilities $\hat{\Pi}$. Note that although the model infers full (Dirichlet) posterior distributions over both the global and local transition probabilities, for clarity here we only show the means of these posterior distributions (indicated by the hat notation). In the example shown, only row 3 of the context transition counts is updated (as context 3 has an overwhelming responsibility at time t), but all rows of the local transition probabilities are updated due to the updating of the global transition probabilities (if the model were non-hierarchical, there would be no global transition probabilities, and so the local transition probabilities would only be updated for context 3 via the updated context transition counts). Thus, inferences about transition probabilities generalise from one context (here context 3) to all other contexts (here

contexts 1 and 2) due to the hierarchical nature of the generative model. Note that when a novel context is encountered for the first time, its local transition probabilities are initialised based on $\hat{\beta}$, thus allowing well-informed inferences about transitions to be drawn immediately. **c-e, Parameter inference in the COIN model for the simulation shown in Fig. 1c-h.** In addition to inferring states and contexts, the COIN model also infers context transition (**c**) and cue (**d**) probabilities, as well as the parameters of context-specific state dynamics (**e**). **c**, Transition probabilities. Top: Inferred global transition probabilities (solid lines) for transitioning into each known context (line colours) and the novel context (grey). Pale lines show inferred stationary probabilities for the same contexts, representing the expected proportion of time spent in each context given the current estimate of the local transition probabilities (below). Bottom three panels: inferred local transition probabilities from each context (colours as in top panel). Note that the local transition probability from context 1 to context 2 increases when cup 3 is handled (that is, when transitions from context 2 to itself are inferred to happen) due to the generalization of inferred transition probabilities across contexts. Also note that the local transition probabilities from context 3 are initialised based on the global transition probabilities (plus a self-transition bias). **d**, Inferred global (top panel) and local cue probabilities for the three known contexts (bottom three panels) and cues (line colours). Although the model infers full (Dirichlet) posterior distributions over both transition (**c**) and cue probabilities (**d**), for clarity here we only show the means of these posterior distributions. **e**, Posterior distributions of the state drift (left) and retention parameters (right) for the three known contexts (colours as in **c**, novel context not shown for clarity). Although the model infers the joint distribution of the drift and retention parameters for each context, for clarity here we show the marginal distribution of each parameter separately. Note that drift and retention are inferred to be larger for the red context that is associated with the largest perturbation.

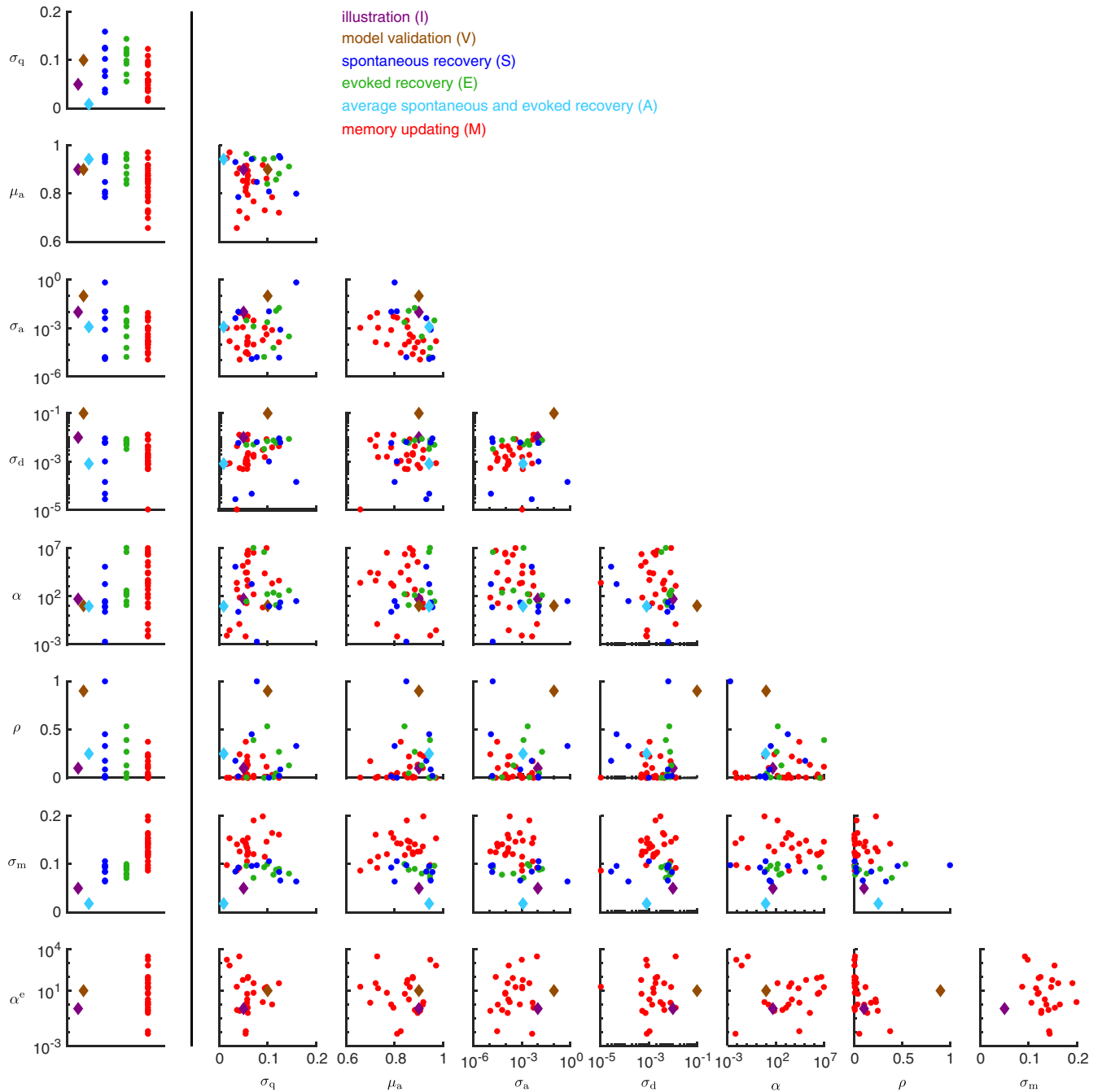
Article



Extended Data Fig. 2 | See next page for caption.

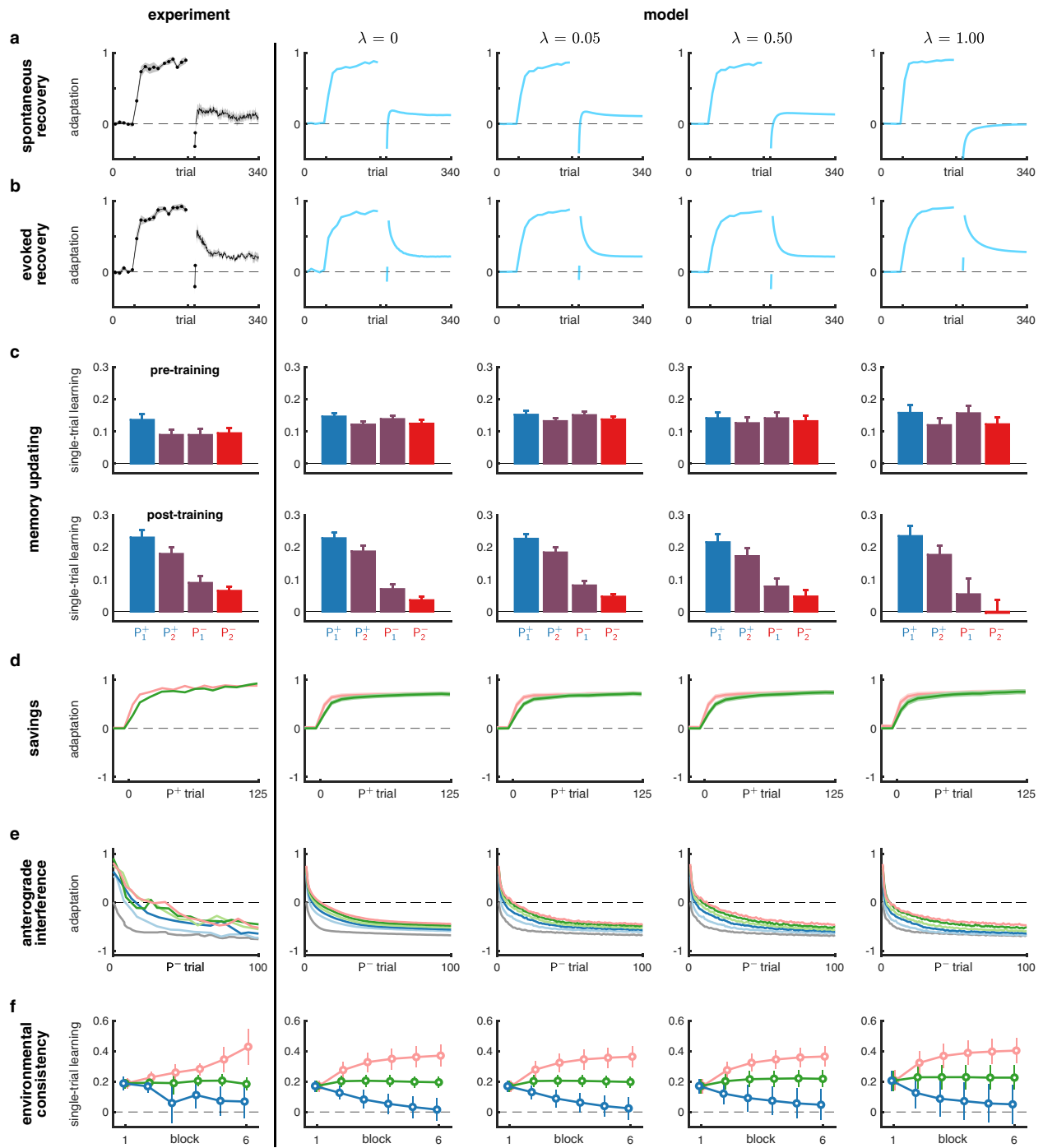
Extended Data Fig. 2 | Validation of the COIN model. a, Validation of the inference algorithm of the COIN model with a single context. We computed inferences in the COIN model with a single context based on synthetic observations (state feedback) generated by its generative model (Fig. 1a). Plots show the cumulative distributions of the posterior predictive p-values for the state variable (left) and the parameters governing its dynamics (retention, middle; drift, right). The posterior predictive p-value is computed by evaluating the cumulative distribution function of the model's posterior over the corresponding quantity at the true value of that quantity (as defined by the generative model). Empirical distributions of the posterior predictive p-values were collected across 4000 simulations (with different true retention and drift parameters), with 500 time steps in each simulation (during which the true state changes, but the true retention and drift parameters are constant). Note that although the true retention and drift parameters do not change during a simulation, inferences in the model about them still evolve in general, and so a new posterior predictive p-value is generated at each time step even for these quantities. If the model implements well-calibrated probabilistic inference under the correct generative model, the empirical distributions of the posterior predictive p-values should all be uniform. This is confirmed by all cumulative distributions of the posterior predictive p-values (orange and purple curves) approximating the identity line (thin black diagonal line). Orange curves show posterior predictive p-values under the corresponding marginals of the model's posterior. To give additional information about the model's joint posterior over the retention and drift parameters, we also show the cumulative distribution of the posterior predictive p-value for each parameter conditioned on the true value of the other parameter (retention | drift, and drift | retention, purple curves). **b, Validation of the inference algorithm of the COIN model with multiple contexts.** Simulations as in **a** but with additional synthetic observations (sensory cues) and multiple contexts allowed both during data generation and inference. Empirical distributions of the posterior predictive p-values were collected across 2000 simulations (with different true retention and drift parameters), with 500 time steps in each simulation (during which not only the true states change but also contexts transition, and sometimes novel contexts become active). Left column shows the true distributions of sensory cues, contexts and parameters. Inset shows the growth of the number of contexts over time both during generation (blue) and inference (orange). Middle and right columns show the cumulative distributions of the posterior predictive p-values (pooled across data sets and time steps) for the observations (top row), contexts and state (middle row) and parameters (bottom row). To calculate the posterior predictive p-values for the

context, inferred contexts were relabelled by minimising the Hamming distance between the relabelled context sequence and the true context sequence (Supplementary Information). For the parameters, the posterior predictive p-values were calculated with respect to both the marginal distributions (retention and drift) and the conditional distributions (retention | drift, and drift | retention) as in **a**. The cumulative probability curves approximate the identity line (thin black diagonal line) showing that the inferred posterior probability distributions are well calibrated. **c, Parameter recovery in the COIN model related to Fig. 2.** Plots show the COIN model parameters that were recovered (y-axes) from fits to 10 synthetic data sets generated with the COIN model parameters (true, x-axes) obtained from the fits to each participant in the spontaneous ($n = 8$) and evoked ($n = 8$) recovery experiments (Extended Data Fig. 3). Vertical bars show the interquartile range of the recovered parameters for each participant. While several parameters are recovered with good accuracy ($\sigma_r, \mu_a, \sigma_d, \sigma_m$), others are not (α , and in particular σ_a and ρ). We expect that with richer paradigms and larger data sets, all parameters would be recovered accurately. Most importantly, despite partial success with recovering individual parameters, model recovery shows that recovered parameter sets taken as a whole can still be used to accurately identify whether data was generated by the dual-rate or COIN model (**d**). Note that we make no claims about individual parameters in this study as our focus is on model class recovery. **d-e, Model recovery for spontaneous (d) and evoked recovery experiments (e) related to Fig. 2.** Synthetic data sets were generated using one of two models (COIN model, cyan; dual-rate model, green). Parameters used for each model were those obtained from the fits to each participant in the spontaneous ($n = 8$) and evoked ($n = 8$) recovery experiments (Extended Data Fig. 3), that is, for the COIN model, these were the same synthetic data sets as those used in **c**. Then the same model comparison method that we used on real data (Fig. 2c, e, insets) was used to recover the model that generated each synthetic data set (Methods). Arrows connect true models (used to generate synthetic data, disks on top) to models that were recovered from their synthetic data (pie-chart disks at bottom). Arrow colour indicates identity of recovered model, arrow thickness and percentages indicate probability of recovered model given true model. Bottom disk sizes and pie-chart proportions show total probability of recovered model and posterior probability of true model given recovered model (assuming a uniform prior over true models), respectively, with percentages specifically indicating posterior probability of the correct model. These results show that the model recovery process is generally very accurate and actually biased against the COIN model in favour of the dual-rate model.



Extended Data Fig. 3 | COIN model parameters. Left column: Parameters for illustrating the COIN model (**I**: purple), model validation (**V**: brown) and fits to individuals in the spontaneous (**S**: blue) and evoked (**E**: green) recovery experiments, to the average of both groups (**A**: cyan), and individuals in the memory-updating experiment (**M**: red). Right: scatter plots for all pairs of parameters for the six groups. The overlap of data points suggest parameters are similar across experiments. σ_q : process noise s.d. (equation 3); μ_a , σ_a : prior mean and s.d. for context-specific state retention factors (equation 10); σ_d : prior s.d. for context-specific state drifts (equation 10); α : concentration of local transition probabilities (equation 8); ρ : self-transition bias parameter (equation 18); σ_m : motor noise s.d. (equation 17); α^e : concentration of local cue probabilities (equation 9). Parameters used in the figures is as follows. **I**: Fig. 1 and Extended Data Fig. 1c–e. **V**: Extended Data Fig. 2a, b. **S**: Fig. 2c, Extended Data Fig. 6f (column 1) and Extended Data Fig. 2d. **E**: Fig. 2e, Extended Data Fig. 6f (column 3) and Extended Data Fig. 2e. **S & E**: Extended Data Fig. 2c.

A: Fig. 2b and d, Extended Data Fig. 5 and Extended Data Fig. 9 (bias added for visuomotor rotation experiments: Extended Data Fig. 5a–j, p–s and Extended Data Fig. 9e–l). **M**: Fig. 3 and Extended Data Fig. 7a–d. **S, E & M**: (all parameters, but α^e): Fig. 4 and Extended Data Fig. 8. The robustness analyses (Extended Data Fig. 4) used perturbed versions of the same parameters as the corresponding unperturbed simulations. To reduce the number of free parameters in the model, we set the parameters of the hierarchical Dirichlet process that determine the expected effective number of contexts or cues, γ (equation 7) and γ^e (equation 9), respectively, both to 0.1, the prior mean for context-specific state drifts μ_d to zero (equation 10) and the standard deviation of the sensory noise σ_s to 0.03 when fitting or simulating the model, with the variance of the observation noise (equations 5 and 19) set to $\sigma_r^2 = \sigma_s^2 + \sigma_m^2$. For visuomotor rotation experiments (Extended Data Fig. 5a–j, p–s and Extended Data Fig. 9e–l), we set the mean of the prior of the bias μ_b to zero (equation 20) and its s.d. σ_b to 70^{-1} .

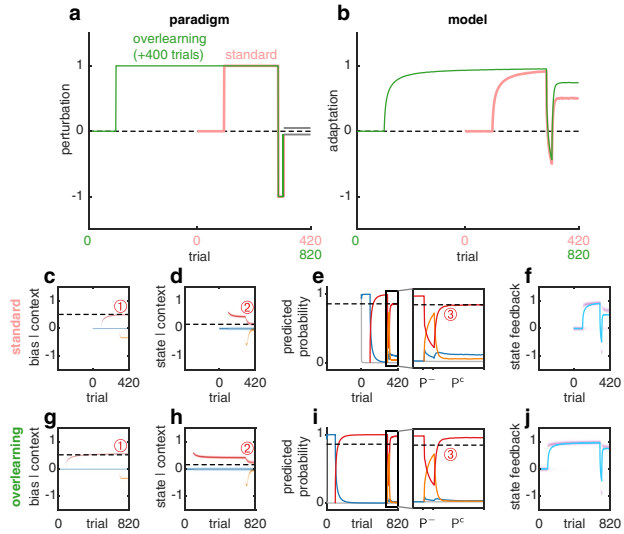


Extended Data Fig. 4 | Robustness analysis of the main COIN model results.

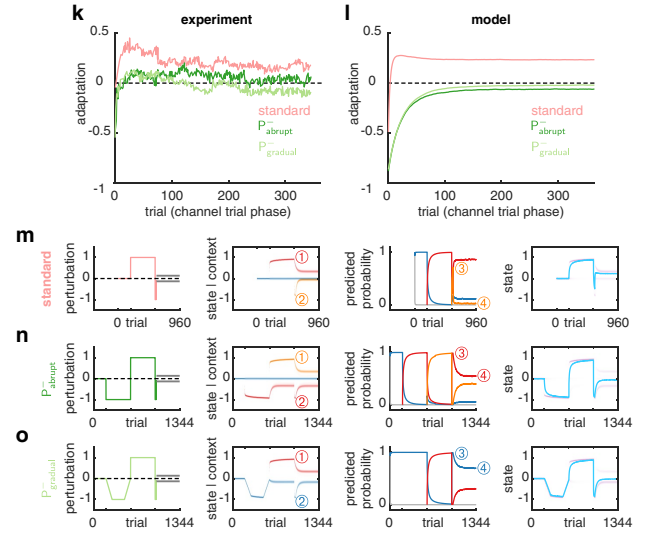
To test how robust the behaviour of the COIN model is, we added noise to the parameters fit to the individual participants in the spontaneous recovery, evoked recovery and memory updating experiments and re-simulated the paradigms in Figs. 2–4: spontaneous recovery (a), evoked recovery (b), memory updating (c), savings (d), anterograde interference (e) and environmental consistency (f). For each experiment, we simulated the COIN model for the same participants as in Figs. 2–4 but perturbed each participant’s parameter values. That is, for each parameter (suitably transformed to be unbounded) we calculated the standard deviation across participants (relevant for the given paradigm or set of paradigms) and then perturbed each participant’s (transformed) parameter by zero-mean Gaussian noise whose standard deviation was a fraction ($\lambda = 0, 0.05, 0.5$ or 1.0) of this empirical standard deviation, after which we used the inverse transform to obtain the actual parameter used in these perturbed simulations. For parameters that are

constrained to be non-negative ($\sigma_q, \sigma_a, \sigma_d, \alpha, \alpha^e, \sigma_m$), we used a logarithmic transformation, whereas for parameters constrained to be on the unit interval (μ_a, ρ), we used a logit transformation. Column 1: experimental data (plotted as in Figs. 2–4). Columns 2–5: output of the COIN model for different amounts of noise added to the parameters. Note that the simulations were not conditioned on the actual adaptation data of individual participants (in contrast to the original simulations of Figs. 2 and 3) because these data are not available for the experiments shown in Fig. 4 (for which the original simulations were already performed using this ‘open-loop’ simulation approach). The robustness analysis shows that most predictions of the COIN model are robust to changes in the parameters and only start to deviate for large parameter changes ($\lambda = 1$) in some of their quantitative details (such as the magnitude of spontaneous recovery). Note that $\lambda = 1$ leads to changes in parameters that are of the same magnitude as randomly shuffling the parameters across participants.

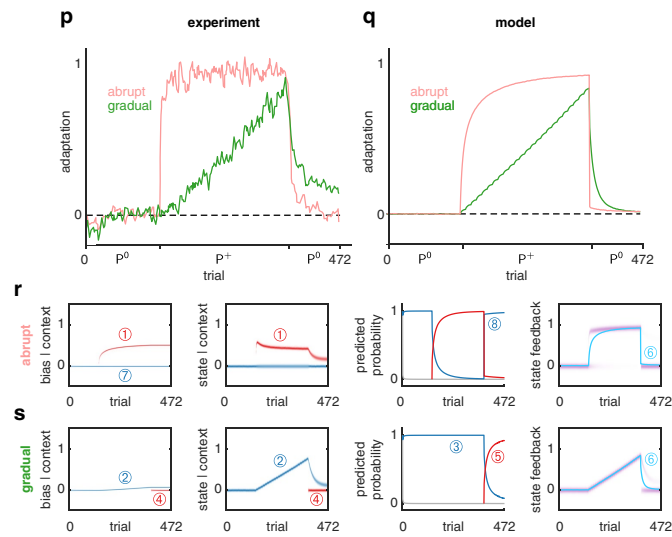
overlearning and spontaneous recovery



pre-training and spontaneous recovery



gradual vs. abrupt perturbations and deadadaptation



Extended Data Fig. 5 | See next page for caption.

Extended Data Fig. 5 | History dependence of contextual inference.

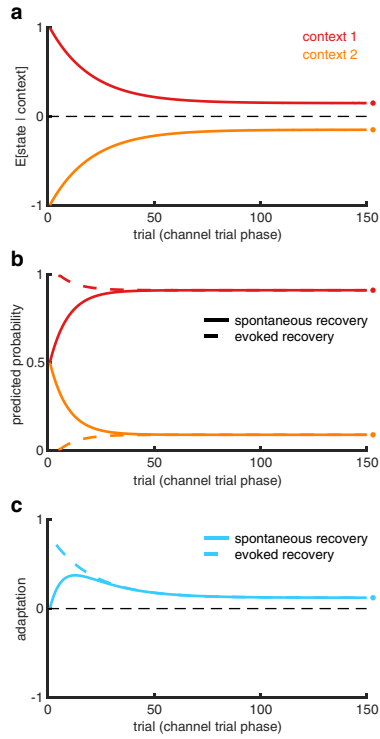
a-j, Contextual inference underlies the elevated level of spontaneous recovery after 'overlearning'.

a, Spontaneous recovery paradigm for visuomotor learning in which the length of the exposure (P^+) phase is tripled from 200 trials ('standard' paradigm, pink) to 600 trials ('overlearning' paradigm, green). For comparison, paradigms are aligned to the end of the exposure phase. **b**, Adaptation in the COIN model for the standard and overlearning paradigms (same parameters as in Fig. 2b and d but with the addition of a bias parameter; see Supplementary Information and also Extended Data Fig. 3, parameter set **A**). Adaptation corresponds to reach angle normalized by the size of the experimentally imposed visuomotor rotation. Note elevated level of spontaneous recovery after overlearning compared to the standard paradigm, qualitatively matching visuomotor learning data in Fig. 4a of Ref. ¹³. **c-f**, Internal representations of the COIN model for the standard paradigm. Inferred bias (**c**) and predicted state (**d**) distributions for each context (colours). **e**, Predicted probabilities of each context (with zoomed view starting from near the end of P^+ exposure), colours as in **c-d**, grey is novel context as in Fig. 1f. **f**, Predicted state feedback (predicted state plus bias) distribution (purple), which is a mixture of the individual contexts' predicted state feedback distributions (not shown) weighted by their predicted probabilities (**e**). Total adaptation (cyan line) is the mean of the predicted state feedback distribution. **g-j**, same as **c-f** for the overlearning paradigm. For comparison, the dashed horizontal lines in both paradigms show the final level of each variable for the red context in the standard paradigm. Note that overlearning leaves inferences about biases and states largely unchanged (compare 1 in **c & g** and 2 in **d & h**) but leads to higher predicted probabilities of the P^+ context (red) in the channel-trial phase (compare 3 in **e & i**), reflecting the true statistics of the experiment in which P^+ occurred more frequently. In turn, this makes the P^+ bias and state contribute more to total adaptation in the channel-trial phase, thus explaining higher levels of spontaneous recovery. Therefore, differences between conditions are explained by contextual inference rather than by differences in bias or state inferences. The results are qualitatively similar when simulated as a force-field paradigm (that is, without bias, not shown). **k-o**, Contextual inference underlies reduced spontaneous recovery following pre-training with P^- . **k**, Adaptation in the channel-trial phase of a typical spontaneous recovery paradigm (standard, pink, as in Fig. 2b) and two modified versions of the paradigm in which the P^+ phase is preceded by a P^- (pre-training) phase in which P^- is either introduced and removed abruptly (P^-_{abrupt} , dark green) or gradually (P^-_{gradual} , light green). Data reproduced from Ref. ¹⁴. **l-o**, Simulation of the COIN model for the same paradigms (same parameters as in Fig. 2b and d; Extended Data Fig. 3, parameter set **A**), plotted

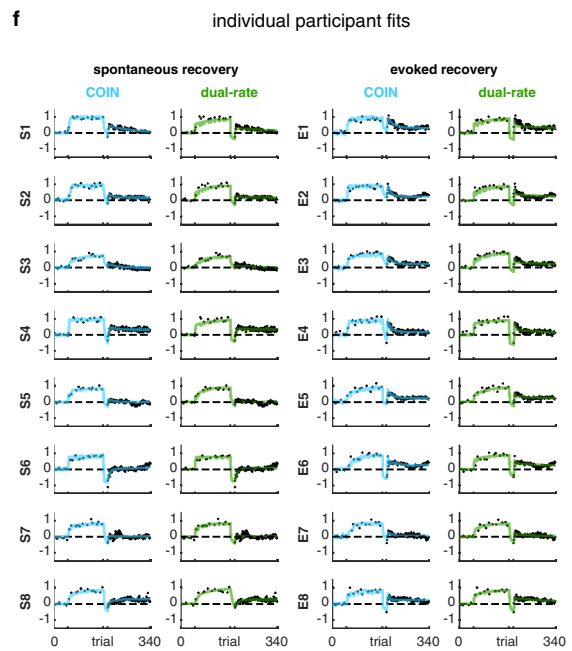
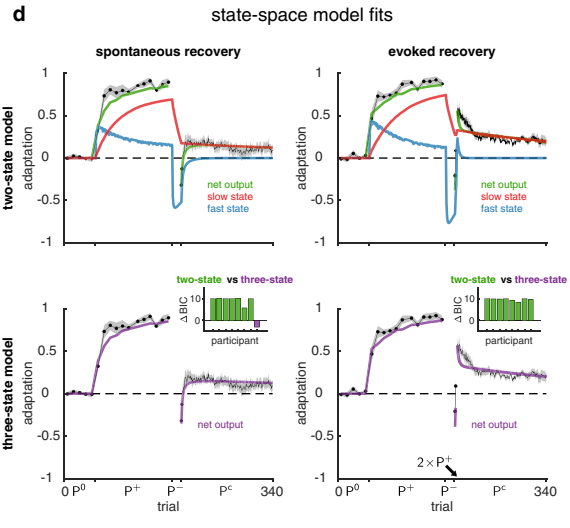
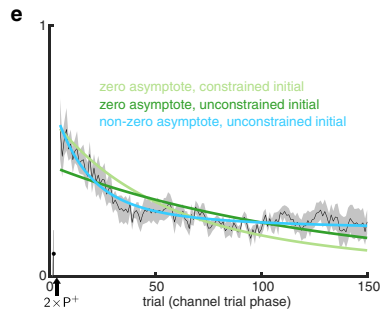
as in Fig. 2b-c. In each paradigm, contexts are coloured according to their order of instantiation during inference (blue \rightarrow red \rightarrow orange). Note that pre-training with P^- (either abrupt or gradual) leaves inferences about states within each context largely unchanged at the beginning of the channel-trial phase (compare corresponding numbers 1-2 in column 2 across **m-o**). However, the pre-training leads to higher predicted probabilities of the P^- context initially (compare number 3 in **m** to number 3 in **n & o**) and throughout the channel-trial phase (compare number 4 across **m-o**) reflecting the true statistics of the experiment in which P^- occurred more frequently (compare column 1 across **m-o**). In turn, this makes the P^- state contribute more to total adaptation, thus explaining the reduction in both the initial and final levels of adaptation during the channel-trial phase in the P^-_{abrupt} and P^-_{gradual} groups. Therefore, as in Fig. 4, differences between conditions are explained by contextual inference rather than state inference. **p-s**, Contextual inference underlies slower de-adaptation following a gradually introduced perturbation.

p, Adaptation (normalized reach angle, as in **b**) in a paradigm in which a visuomotor rotation is introduced abruptly (pink) or gradually (green) and then removed abruptly. Data reproduced from Ref. ¹⁷. **q-s**, Simulation of the COIN model on the abrupt (**q**, pink, and **r**) and gradual (**q**, green, and **s**) paradigms (same parameters as in Fig. 2b and d but with the addition of a bias parameter; Extended Data Fig. 3, parameter set **A**) plotted as in **b-j**. Note that contexts are coloured according to their order of appearance during inference (blue \rightarrow red). In response to the abrupt introduction of the P^+ perturbation, a new memory is created (1). In contrast, the gradual introduction of the P^+ perturbation prevents the creation of a new memory, thus requiring changes in the inferred bias and state of the original memory associated with P^0 (2, blue context) to account for the slowly increasing perturbation. Therefore, the 'blue' context is inferred to be active throughout the exposure phase (3) and becomes associated with a P^+ -like state. However, at the beginning of the abruptly introduced post-exposure (P^0) phase, a new memory is created (4), which has a low initial predicted probability that can only be increased by repeated experience with P^0 (5). This leads to slower de-adaptation in the post-exposure phase compared to the abrupt paradigm (6), in which the original context associated with P^0 (blue) is protected (7) and can be reinstated quickly (8) as the P^0 local self-transition probability has been learned to be higher during the pre-exposure phase. Note that the smaller errors caused by the gradual perturbation relative to the abrupt condition are better accounted for by an error in the state rather than an error in the bias, and therefore the state is updated more than the bias. The results are qualitatively similar when simulated as a force field paradigm (that is, without bias, not shown).

mathematical analysis of spontaneous and evoked recovery



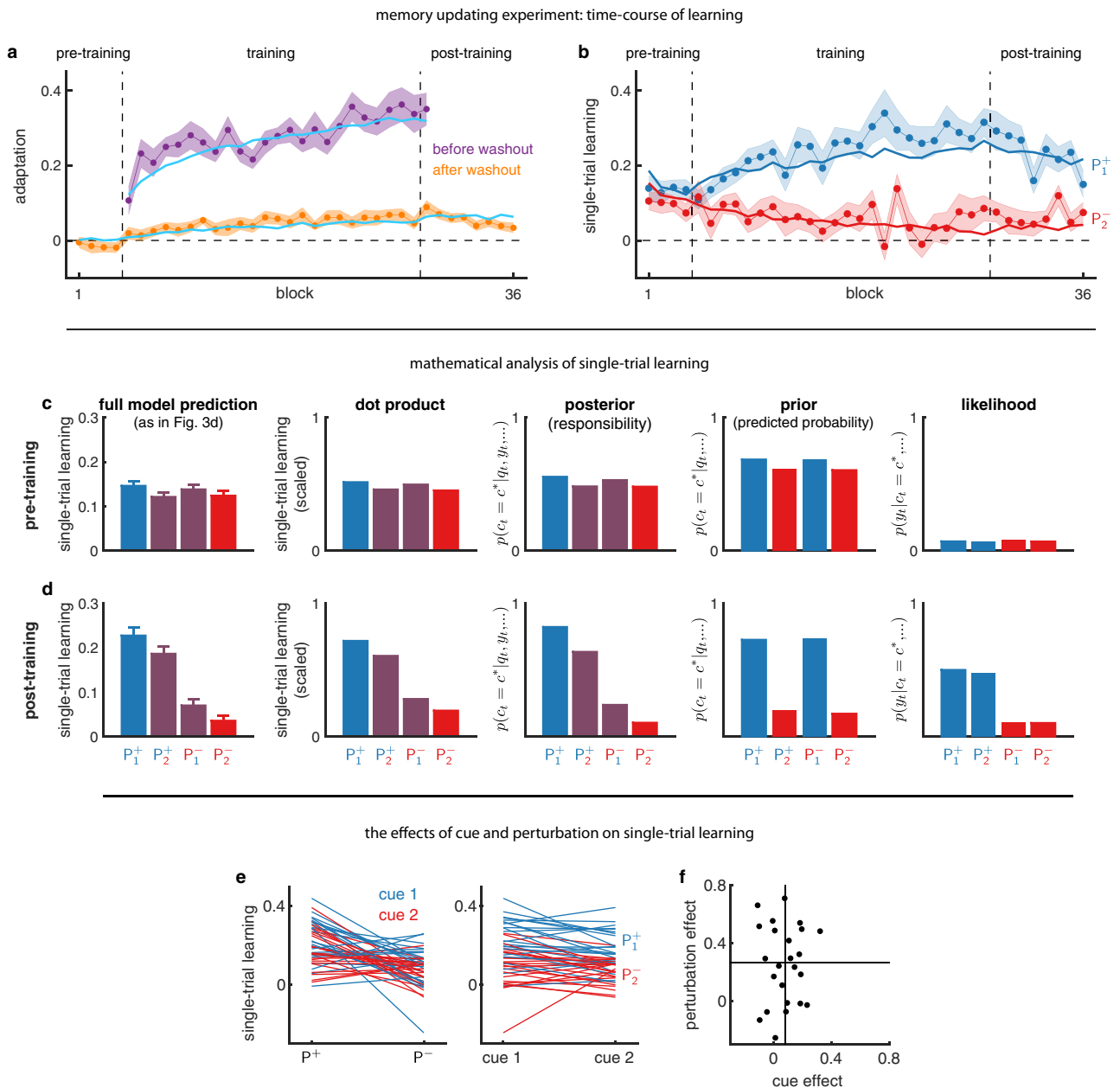
evoked recovery does not decay exponentially to zero



Extended Data Fig. 6 | See next page for caption.

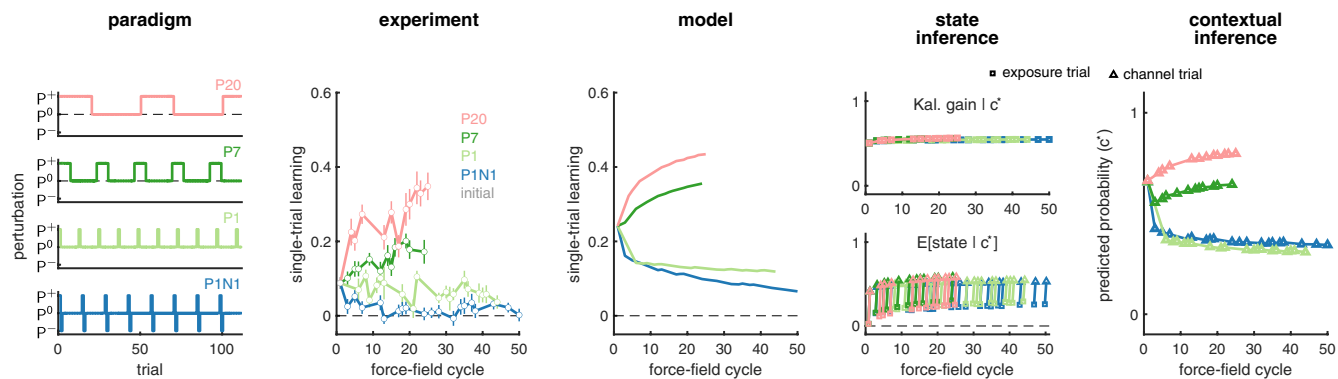
Extended Data Fig. 6 | Additional analyses of spontaneous and evoked recovery related to Fig. 2. a-c, Mathematical analysis of spontaneous and evoked recovery. The channel-trial phase of spontaneous recovery and evoked recovery (after the two P^+ trials) simulated in a simplified setting (Supplementary Information) with two contexts that are initialized to have equal but opposite state estimates (**a**) and equal (spontaneous recovery, solid) or highly unequal (evoked recovery, dashed) predicted probabilities (**b**). For the two contexts, the retention parameters are assumed to be constant and equal, and the drift parameters are assumed to be constant, of the same magnitude but opposite sign. Mean adaptation (**c**), which in the COIN model is the average of the state estimates (**a**) weighted by the corresponding predicted probabilities (**b**), shows the classic pattern of spontaneous recovery (solid, cf. Fig. 2b, c) and the characteristic abrupt rise of evoked recovery (dashed, cf. Fig. 2d, e). Note that although in the full model, state estimates are different between evoked and spontaneous recovery following the two P^+ trials, here we assume they are the same (no separate solid and dashed lines in **a**) for simplicity and to demonstrate that the difference in mean adaptation between the two paradigms (**c**) can be accounted for by differences in contextual inference alone (**b**, cf. Fig. 2b and d, top right). Circles on the right show steady-state values of inferences and adaptation. Note that in both paradigms, adaptation is predicted to decay to a non-zero asymptote (see also **e**). **d, State-space model fits to adaptation data from the spontaneous and evoked recovery groups.** Solid lines show the mean fits across participants of the two-state model (5 parameters, top row) and the three-state model (7 parameters, bottom row) to the spontaneous recovery (left column) and evoked recovery (right column) data sets. Mean \pm s.e.m. adaptation on channel trials shown in black (same as in Fig. 2c and e). Insets show differences in BIC (nats) between the two-state model and the three-state model for individual participants (positive values in green indicate evidence in favour of the two-state model, and negative values in purple indicate evidence in favour of the three-state model). At the group level, the two-state model was far superior to the three-state model (Δ group-level BIC of 64.2 and 78.4 nats in favour of the two-state model for the spontaneous and evoked recovery groups, respectively). Individual states are shown for the two-state model (top, blue and red). Both the fast and slow processes adapt to P^+ during the extended initial learning period. The P^- phase reverses the state of the fast process, but not of the slow process, so that they

cancel when summed resulting in baseline performance. Spontaneous recovery during the P^c phase is then explained by the fast process rapidly decaying, revealing the state of the slow process that has remained partially adapted to P^+ . Note that this explanation arises because in multi-rate models all processes contribute equally to the motor output at all times. This is fundamentally different from the expression and updating of multiple context-specific memories in the COIN model, which are dynamically modulated over time according to ongoing contextual inference. **e, Evoked recovery does not decay exponentially to zero.** According to the COIN model, adaptation in the channel-trial phase of evoked recovery can be approximated by exponential decay to a non-zero (positive) asymptote (**a-c**, Fig. 2e, Supplementary Information). To test this prediction, we fit an exponential function that either decays to zero (light and dark green) or decays to a non-zero (constrained to be positive) asymptote (cyan) to the adaptation data of individual participants in the evoked recovery group after the two P^+ trials (black arrow). The two zero-asymptote models differ in terms of whether they are constrained to pass through the datum on the first trial (light green) or not (dark green). The mean fits across participants for the models that decay to zero (green) fail to track the mean adaptation (black, \pm s.e.m. across participants), which shows an initial period of decay followed by a period of little or no decay. The mean fit for the model that decays to a non-zero asymptote (cyan) tracks the mean adaptation well and was strongly favoured in model comparison (Δ group-level BIC of 944.3 and 437.7 nats compared to the zero-asymptote fits with constrained and unconstrained initial values, respectively). Note that fitting to individual participants excludes the confound of finding a more complex time course (e.g. one with a non-zero asymptote) only due to averaging across participants that each show a different simple time course (e.g. all with zero asymptote but different time constants). **f, COIN and dual-rate model fits for individual participants in the spontaneous and evoked recovery groups.** Data and model predictions are shown for individual participants as in Fig. 2c and e for across-participant averages. Participants in the **S** and **E** groups are ordered by decreasing BIC difference between the dual-rate and COIN model (that is, **S1**'s and **E1**'s data most favour the COIN model), as in insets of Fig. 2c and e. Note that the COIN model can account for much of the heterogeneity of spontaneous recovery (e.g. from large in **S1** to minimal in **S6**) and evoked recovery (e.g. from large in **E1** to minimal in **E7**).



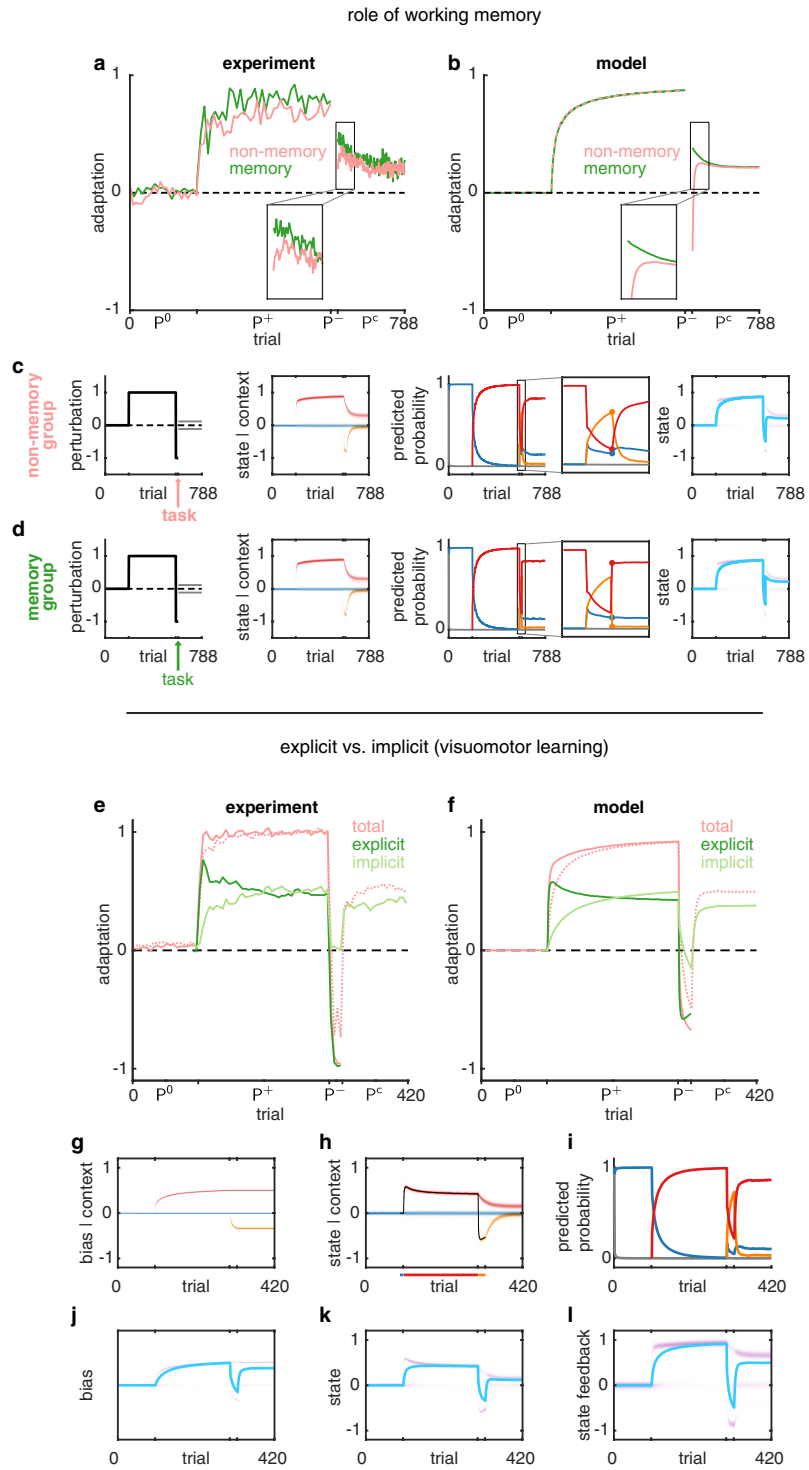
Extended Data Fig. 7 | Additional analyses of the memory updating experiment (related to Fig. 3). a-b, Memory updating experiment: time-course of learning. **a**, Adaptation on channel trials at the end of each block of force-field trials in the training phase (purple), which occur before P^0 washout trials, and on the first channel trial of triplets within each block (orange), which occurs after P^0 washout trials. Data is mean \pm s.e.m. across participants and lines show mean of COIN model fits (8 parameters, Extended Data Fig. 3). **b**, Single-trial learning on triplets that were consistent with the training contingencies. Data (mean \pm s.e.m. across participants) with mean of COIN model fits across participants. Positive learning reflects changes in the direction expected based on the force field of the exposure trial (an increase following P^+ and a decrease following P^-). **c-d, Mathematical analysis of single-trial learning.** Single-trial learning in the COIN model (column 1) for the four cue-perturbation triplets in the pre-training phase (**c**) and the post-training phase (**d**) in the memory updating experiment. The COIN model was fit to each participant and model fits are shown as mean \pm s.e.m. (single-trial learning, full model prediction) or mean (dot product, posterior, prior and likelihood) across $n = 24$ participants. Single-trial learning (column 1) is approximately proportional to a dot product (column 2) between the vector of posterior context probabilities (responsibilities) on the exposure trial of the triplet and the vector of predicted context probabilities on the subsequent channel trial (see the Supplementary Information for derivation). This dot

product can be further approximated by collapsing the vector of predicted probabilities to a one-hot vector, that is, by the responsibility $p(c_t = c^* | q_t, y_t, \dots)$ (column 3) of the context that is predominantly expressed on the second channel trial of the triplet (c^* , the context with the highest predicted probability on the second channel trial of the triplet), where ... denotes all observations before time t (as in Fig. 1). This responsibility is proportional to a product of two terms. The first term is the prior context probability $p(c_t = c^* | q_t, \dots)$ (column 4), that is, the predicted context probability before experiencing the perturbation (as in Fig. 1f), which is already conditioned on the sensory cue visible from the outset of the trial. The second term expresses the likelihood of the state feedback in that context $p(y_t | c_t = c^*, \dots)$ (column 5). Because prior to learning neither cues nor feedback are yet consistently associated with a particular context, the COIN model predicts that the prior and likelihood, and thus total single-trial learning should all be largely uniform across contexts before training. **e-f, The effects of cue and perturbation on single-trial learning in individual participants.** **e**, Single-trial learning (post-training) shown as a function of perturbation separated by cue (left) or as a function of cue separated by perturbation (right) for each participant (lines). Note a significant effect for both the perturbation and the cue. **f**, Scatter plot of cue effect ($P_1^+ + P_1^- - P_2^+ - P_2^-$) against perturbation effect ($P_1^+ + P_2^+ - P_1^- - P_2^-$) for each participant (dots). Solid lines show medians of corresponding effects. Note the lack of anti-correlation between two effects.



Extended Data Fig. 8 | Additional analysis of the effect of environmental consistency on single-trial learning related to Fig. 4c. Columns 1 & 2: experimental paradigm and data replotted from Ref. ⁵. Participants experienced repeating cycles of P^+ trials of varying lengths (column 1: 20 P^+ trials in P20, 7 in P7, 1 in P1 and 1 followed by 1 P^- trial in P1N1) in between P^0 trials. To assess single-trial learning (column 2) during exposure to the environments, channel trials were randomly interspersed before and after the first P^+ trial in a subset of the force-field cycles. Columns 3 to 5 show the output and internal

inferences of the COIN model in the same format as Fig. 4c (same parameters as in Fig. 4; Extended Data Fig. 3, parameter set **S, E & M**). The COIN model qualitatively reproduced the pattern of changes in single-trial learning seen over repeated cycles in this paradigm. As in Fig. 4, differences in the apparent learning rate were not driven by differences in either the proper learning rate (Kalman gain) or the underlying state (column 4) but were instead driven by changes in contextual inference (column 5).



Extended Data Fig. 9 | See next page for caption.

Extended Data Fig. 9 | Cognitive processes and the COIN model.

a-d, Maintenance of context probabilities may require working memory.

a, Adaptation in a spontaneous recovery paradigm in which a non-memory (pink) or working memory task (green) is performed at the end of the P^c phase before starting the channel-trial phase (data reproduced from Ref. ²³). Initial adaptation in the channel-trial phase (inset) shows the working memory task abolishes spontaneous recovery and leads to adaptation akin to evoked recovery (cf. Extended Data Fig. 6a–c). **b-d**, COIN model simulation in which the working memory task abolishes the (working) memory of the context responsibilities on the last trial of the P^c phase but not the context transition (and thus stationary) probabilities (same parameters as in Fig. 2b and d; Extended Data Fig. 3, parameter set **A**), plotted as in Fig. 2b, c. The circles on the predicted probability (zoomed view) show the values on the first trial in the channel-trial phase. **d**, as (c) but for the working memory task. The predicted probabilities on the first trial in the channel-trial phase are set to the values under the stationary distribution (shown on every trial in the simulation of Extended Data Fig. 1c). We calculate the stationary context distribution by solving $\psi = \psi \hat{\Gamma}$ for ψ (a row vector), subject to the constraint that ψ is a valid probability distribution (i.e. all elements of ψ are non-negative and sum to 1), where $\hat{\Gamma}$ is the expected local transition probability matrix. **e-l, Explicit versus implicit learning in the COIN model.** **e**, Results of a spontaneous recovery paradigm (as in Fig. 2b) for visuomotor learning. Adaptation is computed as participants' reach angle normalized by the size of the experimentally imposed visuomotor rotation. Explicit learning (dark green) is measured by participants indicating their intended reach direction. Implicit learning (light green) is

obtained as the difference between total adaptation (solid pink) and explicit learning. In the visual error-clamp phase (P^c), participants were told to stop using any aiming strategy so that the direction they moved was taken as the implicit component of learning. A control experiment (dashed pink) was also performed in which there was no reporting of intended reach direction. Data reproduced from Ref. ²⁴. **f-l**, Simulation of the COIN model on the same paradigm (same parameters as in Fig. 2b and d but with the addition of a bias parameter; Extended Data Fig. 3, parameter set **A**). **b**, Predictions for experimentally observable quantities. Light green line: implicit learning is the average bias across contexts weighted by the predicted probabilities (cyan line in **j**). Dark green line: explicit learning is the state of the most responsible context on the previous trial (black line in **h**). Solid pink line: total adaptation for the reporting condition is the sum of explicit and implicit learning (as in **e**). Dashed pink line: total adaptation for the non-reporting condition is the average predicted state feedback across contexts weighted by the predicted probabilities (cyan line in **l**, as in all experiments that had no reporting element). **g-h**, Inferred bias (**g**) and predicted state (**h**) distributions for each context (colours), with black line showing the mean state of the most responsible context (coloured line below axis) for trials on which an explicit report was solicited. **i**, Predicted probability of each context. Colours as in **g-h**, grey is novel context as in Fig. 1f. **j-k**, Inferred bias (**j**) and predicted state (**k**) distributions (purple), obtained as mixtures of the respective distributions of individual contexts (**g-h**) weighted by their predicted probabilities (**i**), and their means (cyan lines). **l**, Predicted state feedback distribution (purple, computed as the sum of bias in **j** and predicted state in **k**) and its mean (cyan).

Extended Data Table 1 | Comparison of the COIN model to other models

	single-context models		multiple-context models				
	dual-rate	memory of errors	source of errors	winner-take-all	DP-KF	MOSAIC	COIN
	Smith et al. ¹	Herzfeld et al. ⁴	Berniker & Körding ¹⁶	Oh & Schweighofer ¹¹	Gershman et al. ¹²	Haruno et al. ²⁶	
spontaneous recovery	✓	✗ ^a	✗ ^b	✗ ^b	✗ ^c	✗ ^d	✓
evoked recovery	✗ ^e	✗ ^e	✗ ^f	✗ ^f	✗ ^f	✗ ^d	✓
memory updating	✗ ^g	✗ ^g	✗ ^g	✗ ^h	✗ ^{g,h}	✓	✓
savings after full washout	✗ ⁱ	✓	✓	✓	✓	✓	✓
anterograde interference	✓	✗ ^a	✗ ^b	✗ ^b	✓	✗ ^j	✓
environmental consistency	✗ ⁱ	✓	✗ ^b	✗ ^b	✗ ^k	✓	✓
explicit/implicit learning	✗ ^m	✗ ^l	✗ ^l	✗ ^l	✗ ^l	✗ ^l	✓

Table shows which experimental phenomena (rows) can be explained by different single and multiple-context models (columns). Alphabetical superscripts index the key feature(s) missing from each model that are primarily responsible for their inability to explain a particular phenomenon. Note that we consider each model as described and implemented by its authors (although it might be possible to modify or extend these models to explain more features). Orange cross-ticks are for models that can partially explain a phenomenon. **Spontaneous recovery**, the gradual re-expression of P^+ in the channel-trial phase (Fig. 2c), requires a single-context model to have multiple states that decay on different time scales or a multiple-context model that can change the expression of memories in a gradual manner based on the amount of experience with each context. Therefore, single-context models that have a single state^a, or multiple-context models that do not learn context transition probabilities^b or do not have state dynamics^d do not show spontaneous recovery. Models that learn transition probabilities but that do not represent uncertainty about the previous context^e (the ‘local’ approximation in DP-KF) can either include a self-transition bias or not. With a self-transition bias, the expression of memories changes in an abrupt manner (akin to evoked recovery) when, in the channel-trial phase, the belief about the previous context changes (e.g. from P^- to P^+), and thus such models fail to explain the gradual nature of spontaneous recovery. Without a self-transition bias, the change in expression of memories is gradual based on updated context counts, but this occurs too slowly relative to the time scale on which the rise of spontaneous recovery occurs. **Evoked recovery**, the rapid re-expression of the memory of P^+ in the channel-trial phase (Fig. 2e) that does not simply decay exponentially to baseline (Extended Data Fig. 6e), requires a model to be able to switch between different memories based on state feedback. Therefore, single-context models^a that cannot switch between memories are unable to show the evoked recovery pattern seen in the data. Multiple-context models with memories that decay exponentially to zero in the absence of observations^f (for example, during channel trials) can only partially explain evoked recovery, showing the initial evocation but not the subsequent change in adaptation over the channel-trial phase. Models with no state decay^d cannot explain evoked recovery. **Memory updating** requires a model to update memories in a graded fashion and to use sensory cues to compute these graded updates. Therefore, models that either have no concept of sensory cues^g or multiple-context models that only update the state of the most probable context in an all-or-none manner^h do not show graded memory updating. **Savings**, faster learning during re-exposure compared to initial exposure after full washout, requires a single-context model to increase its learning rate or a multiple-context model to protect its memories from washout and/or learn context transition probabilities. Therefore, single-context models with fixed learning ratesⁱ do not show savings. **Anterograde interference**, increasing exposure to P^+ leads to slower subsequent adaptation to P^- , requires a single-context model to learn on multiple time scales or a multiple-context model to learn transition probabilities that generalise across contexts. Therefore, single-context models with a single state^a, or multiple-context models that either do not learn transition probabilities^b or that learn local transition probabilities independently for each row of the transition probability matrix^j do not show anterograde interference. **Environmental consistency**, the increase/decrease in single-trial learning for slowly/rapidly switching environments, requires a model to either adapt its learning rate or learn local transition probabilities based on context transition counts. Therefore, single-context models with fixed learning ratesⁱ or multiple-context models that either do not learn transition probabilities^b or that learn non-local transition probabilities based only on context counts^k do not show the effects of environmental consistency on single-trial learning. **Explicit and implicit learning**, the decomposition of visuomotor learning into explicit and implicit components, requires a model to have elements that can be mapped onto these components. For most models, there is no clear way to map model elements onto these components^l. It has been suggested that the fast and slow processes of the dual-rate model may correspond to the explicit and implicit components of learning, respectively. However, in a spontaneous recovery paradigm, this mapping only holds during initial exposure and fails to account for the time course of the implicit component during the counter-exposure and channel-trial phases^m (Supplementary Information).

Reporting Summary

Nature Research wishes to improve the reproducibility of the work that we publish. This form provides structure for consistency and transparency in reporting. For further information on Nature Research policies, see our [Editorial Policies](#) and the [Editorial Policy Checklist](#).

Statistics

For all statistical analyses, confirm that the following items are present in the figure legend, table legend, main text, or Methods section.

n/a Confirmed

- The exact sample size (n) for each experimental group/condition, given as a discrete number and unit of measurement
- A statement on whether measurements were taken from distinct samples or whether the same sample was measured repeatedly
- The statistical test(s) used AND whether they are one- or two-sided
Only common tests should be described solely by name; describe more complex techniques in the Methods section.
- A description of all covariates tested
- A description of any assumptions or corrections, such as tests of normality and adjustment for multiple comparisons
- A full description of the statistical parameters including central tendency (e.g. means) or other basic estimates (e.g. regression coefficient) AND variation (e.g. standard deviation) or associated estimates of uncertainty (e.g. confidence intervals)
- For null hypothesis testing, the test statistic (e.g. F , t , r) with confidence intervals, effect sizes, degrees of freedom and P value noted
Give P values as exact values whenever suitable.
- For Bayesian analysis, information on the choice of priors and Markov chain Monte Carlo settings
- For hierarchical and complex designs, identification of the appropriate level for tests and full reporting of outcomes
- Estimates of effect sizes (e.g. Cohen's d , Pearson's r), indicating how they were calculated

Our web collection on [statistics for biologists](#) contains articles on many of the points above.

Software and code

Policy information about [availability of computer code](#)

Data collection Custom code written in C++ for the vBOT robotic interface

Data analysis MATLAB R2020a.

For manuscripts utilizing custom algorithms or software that are central to the research but not yet described in published literature, software must be made available to editors and reviewers. We strongly encourage code deposition in a community repository (e.g. GitHub). See the Nature Research [guidelines for submitting code & software](#) for further information.

Data

Policy information about [availability of data](#)

All manuscripts must include a [data availability statement](#). This statement should provide the following information, where applicable:

- Accession codes, unique identifiers, or web links for publicly available datasets
- A list of figures that have associated raw data
- A description of any restrictions on data availability

All data, code, and materials used in the analysis are available in a public repository as documented in the paper

Field-specific reporting

Please select the one below that is the best fit for your research. If you are not sure, read the appropriate sections before making your selection.

Life sciences Behavioural & social sciences Ecological, evolutionary & environmental sciences

For a reference copy of the document with all sections, see [nature.com/documents/nr-reporting-summary-flat.pdf](https://www.nature.com/documents/nr-reporting-summary-flat.pdf)

Behavioural & social sciences study design

All studies must disclose on these points even when the disclosure is negative.

Study description	Study of human motor learning with quantitative measurements using a robotic interface
Research sample	Participants has to be age 18-45 with no problems affecting the control of movement and right handed. 40 neurologically-healthy participants participated (18 males and 22 females; age 27.7 +/- 5.6 yr, mean +/- s.d.). Sample sizes were representative chosen on the basis of the typical between-participant variability observed in similar motor adaptation studies (e.g. Herzfeld 2014, Smith 2006, Heald 2018, McDougle 2015- see main text for references).
Sampling strategy	Participants were randomly allocated to groups.
Data collection	Data was collected with a vBOT robotic interface - only the participant and experimenter were present and the experimenter was not blind to the hypothesis being tested.
Timing	Data was collected between May 2018 and May 2019
Data exclusions	No data was excluded
Non-participation	No participants dropped out
Randomization	Allocation into experimental groups was random

Reporting for specific materials, systems and methods

We require information from authors about some types of materials, experimental systems and methods used in many studies. Here, indicate whether each material, system or method listed is relevant to your study. If you are not sure if a list item applies to your research, read the appropriate section before selecting a response.

Materials & experimental systems

- | n/a | Involvement in the study |
|-------------------------------------|---|
| <input checked="" type="checkbox"/> | <input type="checkbox"/> Antibodies |
| <input checked="" type="checkbox"/> | <input type="checkbox"/> Eukaryotic cell lines |
| <input checked="" type="checkbox"/> | <input type="checkbox"/> Palaeontology and archaeology |
| <input checked="" type="checkbox"/> | <input type="checkbox"/> Animals and other organisms |
| <input type="checkbox"/> | <input checked="" type="checkbox"/> Human research participants |
| <input checked="" type="checkbox"/> | <input type="checkbox"/> Clinical data |
| <input checked="" type="checkbox"/> | <input type="checkbox"/> Dual use research of concern |

Methods

- | n/a | Involvement in the study |
|-------------------------------------|---|
| <input checked="" type="checkbox"/> | <input type="checkbox"/> ChIP-seq |
| <input checked="" type="checkbox"/> | <input type="checkbox"/> Flow cytometry |
| <input checked="" type="checkbox"/> | <input type="checkbox"/> MRI-based neuroimaging |

Human research participants

Policy information about [studies involving human research participants](#)

Population characteristics	see above
Recruitment	Human volunteers from the local Cambridge community or the local Columbia and Manhattan community.
Ethics oversight	Columbia University IRB and Cambridge Psychology ethics committee

Note that full information on the approval of the study protocol must also be provided in the manuscript.